

## THE FIRST DETECTIONS OF THE EXTRAGALACTIC BACKGROUND LIGHT AT 3000, 5500, AND 8000Å (II): MEASUREMENT OF FOREGROUND ZODIACAL LIGHT

REBECCA A. BERNSTEIN<sup>1,2,3</sup>

WENDY L. FREEDMAN<sup>2</sup>

BARRY F. MADORE<sup>2,4</sup>

- 1) Division of Math, Physics, and Astronomy, California Institute of Technology, Pasadena, CA 91125
- 2) Carnegie Observatories, 813 Santa Barbara St, Pasadena, CA 91101
- 3) rab@ociw.edu, Hubble Fellow
- 4) NASA/IPAC Extragalactic Database, California Institute of Technology, Pasadena, CA 91125

*Submitted: 13 June 2000 ; Revised: 2 November 2001*

### ABSTRACT

We present a measurement of the absolute surface brightness of the zodiacal light (3900–5100Å) toward a fixed extragalactic target at high ecliptic latitude based on moderate resolution ( $\sim 1.3\text{\AA}$  per pixel) spectrophotometry obtained with the du Pont 2.5m telescope at Las Campanas Observatory in Chile. This measurement and contemporaneous Hubble Space Telescope data from WFPC2 and FOS comprise a coordinated program to measure the mean flux of the diffuse extragalactic background light (EBL). The zodiacal light at optical wavelengths results from scattering by interplanetary dust, so that the zodiacal light flux toward any extragalactic target varies seasonally with the position of the Earth. This measurement of zodiacal light is therefore relevant to the specific observations (date and target field) under discussion. To obtain this result, we have developed a technique that uses the strength of the zodiacal Fraunhofer lines to identify the absolute flux of the zodiacal light in the multiple-component night sky spectrum. Statistical uncertainties in the result are 0.6% ( $1\sigma$ ). However, the dominant source of uncertainty is systematic errors, which we estimate to be 1.1% ( $1\sigma$ ). We discuss the contributions included in this estimate explicitly. The systematic errors in this result contribute 25% in quadrature to the final error in our coordinated EBL measurement, which is presented in the first paper of this series.

*Subject headings:* Diffuse radiation — cosmology: observations — techniques: spectroscopic — interplanetary medium

### 1. INTRODUCTION

This is the second in a series of three papers in which we present a measurement of the mean flux of the optical extragalactic background light and the cosmological implications of that result (see Bernstein, Freedman, & Madore 2002a & 2002c). The extragalactic background light (EBL) is the spatially averaged surface brightness of all extragalactic sources, resolved and unresolved. As such, the absolute flux of the EBL is a powerful and fundamental cosmological constant which can significantly constrain galaxy formation and evolution scenarios. Like all diffuse backgrounds, however, the optical EBL is very difficult to isolate from foreground sources, which are two orders of magnitude brighter. At high Galactic and ecliptic latitudes ( $> 30^\circ$ ), the sky flux observed from the ground is dominated by terrestrial airglow and zodiacal light (ZL), each with a surface brightness of  $\sim 23$  AB mag  $\text{arcsec}^{-2}$ . The Hubble Space Telescope (HST), which orbits at an altitude of 600 km, avoids atmospheric emission, but the total sky flux is still dominated by ZL. An accurate measurement of the ZL is therefore crucial to a successful detection of the diffuse EBL.

Our measurement of the EBL involves simultaneous HST and ground-based observations. From HST we measure the total flux of the night sky, including ZL. Using spectrophotometry over the range 3860–5150Å (1.25Å per pixel) taken with the Boller & Chivens Spectrograph on the duPont 2.5m Telescope at Las Campanas Observatory in Chile, we measure the absolute flux of the ZL contribut-

ing to the HST observations, which we can then subtract. In Bernstein, Freedman, & Madore (2002a, henceforth Paper I), we present the full details of the coordinated program to measure the EBL. In this paper, we present the ground-based measurement of the absolute flux of the ZL. As calibration of these data is crucial to the scientific goals, the data acquisition, reduction, and flux calibration are discussed here in detail.

Background regarding the nature of the ZL is given in §2. The observations, data reduction, and flux calibration are discussed in §3. In §4, we briefly described the complications which arise due to atmospheric scattering, which redirects off-axis flux into and on-axis flux out of the line of sight. Detailed calculations of the atmospheric scattering relevant to precisely our observing situation (defined by the observatory location and positions of the Sun, Galaxy, and target relative to each other and the horizon) are relegated to the Appendix, and summarized in §4. In §5, we describe the technique used to measure the zodiacal light flux in reduced spectra. The results are summarized in §6.

### 2. BACKGROUND

Zodiacal light (ZL) is sunlight scattered off of dust grains in the solar system. Dust column densities are largest toward the ecliptic plane, causing the highest ZL intensities there. The scattering geometry is illustrated in Figure 1 for a high latitude field viewed near the anti-solar direction. The figure shows the scattering angle and line of

sight as defined by geocentric ecliptic longitude ( $\lambda - \lambda_{\odot}$ , in which  $\lambda$  is ecliptic longitude) and ecliptic latitude ( $\beta$ ). At ecliptic latitudes greater than 30 degrees and large scattering angles, the zodiacal light can be as faint as  $\sim 23$  mag arcsec $^{-2}$  at 5000Å ( $\sim 1 \times 10^{-7}$  ergs s $^{-1}$  cm $^{-2}$  sr $^{-1}$  Å $^{-1}$ ) with a solar-type spectrum. In the ecliptic plane and near the Sun, the ZL can be as much as 20 times brighter than at high ecliptic latitudes and significantly reddened relative to the incident solar spectrum. The positional dependence of the ZL flux and color is a function of the density and composition of the scattering particles and of scattering geometry such that the zodiacal light is redder and brighter at smaller elongation angles (see Leinert *et al.* 1998). In general, the solar spectrum is preserved in the spectrum of the ZL with less than 30% deviation in the broad-band spectral shape from the UV to the near-IR (0.2 – 2 $\mu$ m).

Such weakly wavelength-dependent scattering can be characterized by simple Mie scattering theory, which generally describes the interaction of photons with solid particles larger than the wavelength of the incident light (Röser & Staude 1978). The interplanetary dust (IPD) cloud at the orientations of interest to us is known to be composed predominantly of particles larger than 10 $\mu$ m with moderate surface roughness and layered composition. These conclusions are based on IR observations of the thermal properties of the IPD, dynamical arguments, and laboratory work on dust captured in the upper atmosphere and on the moon (see Reach *et al.* 1996; Berriman *et al.* 1994, Dermott *et al.* 1996; Brownlee 1978; Fechtig *et al.* 1974; Leinert *et al.* 1998 and references therein). In the absence of free electrons, the cross-sections for non-linear scattering, such as Raman scattering or two-photon processes, are too low to be a significant effect for dust particles with large dielectric constants.

Indeed, Mie scattering models for rough particles with the size and composition of the IPD successfully describe the weakly wavelength-dependent scattering characteristic of the ZL: the incident spectrum is slightly reddened over very broad band-passes, while narrow-band spectral features are preserved to high precision (Weiss-Wrana 1983, Schiffer 1985). Both these narrow- and broad-band characteristics have been empirically demonstrated, as the ZL spectrum is seen to be roughly 5-10% redder per 1000Å over the range from 3000-8000Å than the Sun (see Leinert *et al.* 1998 and references therein), and Beggs *et al.* (1964) have shown that the Fraunhofer lines in the ZL show no measurable deviation from their solar equivalent widths to the accuracy of their calibration (2%). The broad-band reddening is characterized as the color of the ZL relative to the solar spectrum as a function of wavelength,

$$C(\lambda, \lambda_0) = \frac{I_{ZL}(\lambda)/I_{\odot}(\lambda)}{I_{ZL}(\lambda_0)/I_{\odot}(\lambda_0)}. \quad (1)$$

While Mie scattering explains the spectrum and intensity of the ZL in general, the exact flux of the ZL cannot be modeled to the accuracy we require here, simply due to uncertainties in the exact composition and column density of the IPD. Empirically, the surface brightness of the ZL is known to roughly 10% accuracy as a function of scattering geometry and ecliptic latitude alone. However, uncertainty in flux calibrations of those surface brightness measurements and spatial variability in the IPD cloud

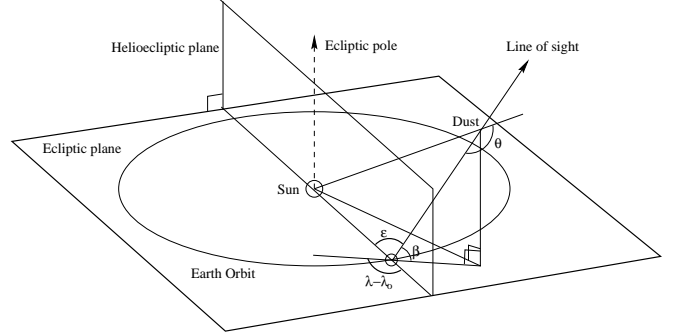


FIG. 1.— The geometry of zodiacal light scattering (adapted from Matsuura, Matsumoto, & Matsuura 1995). The viewing line of sight is defined by ecliptic latitude ( $\beta$ ), and geocentric ecliptic longitude, ( $\lambda - \lambda_{\odot}$ ), or alternatively, by  $\beta$  and the elongation angle,  $\epsilon$ , which is defined as  $\cos \epsilon = \cos(\lambda - \lambda_{\odot}) \cos \beta$ . The scattering angle is  $\theta$ .

(such as cometary trails) preclude more accurate predictions (Levasseur-Regourd & Dumont 1980; Richter *et al.* 1982; Leinert *et al.* 1998 and references therein). In addition, most published measurements of the ZL flux include the background EBL in the reported surface brightness of the ZL. In order to detect the EBL, we must explicitly measure the zodiacal contribution to the sky surface brightness along a specific line of sight at a particular wavelength.

In order to uniquely define the ZL spectrum, both the mean flux in a narrow-bandpass and the broad-band color over the wavelength range of interest must be measured for the line of sight in question. We can do so by making use of the fact that the equivalent widths of solar Fraunhofer lines, reproduced in the ZL spectrum, are known to very high accuracy: we can then determine the continuum level (mean flux) of the ZL at a given wavelength by measuring the apparent equivalent width of the Fraunhofer in spectrum of the night sky. For example, if the equivalent width of the Fraunhofer lines in the night sky around 4500Å are only one half the strength of the same absorption features in the solar spectrum, then the ZL contributes only 50% of the night sky flux at that wavelength. A practical complication of this approach is, of course, identifying the continuum level for accurate measurement of the equivalent widths. Because the ZL and atmospheric emission (airglow) contribute almost equally to the night sky flux in the visible wavelength range at the ecliptic orientation of our observations, this becomes prohibitively difficult where airglow lines become strong (above 5500Å). The problem is further complicated by the fact that the airglow spectrum is continually changing, both in the strength of particular lines and in its mean, wide-band flux. In order to accomplish this measurement, we have therefore developed a new technique for deconvolving one known signal from a variable, multicomponent spectrum. The details of this technique are discussed in §5.

### 3. OBSERVATIONS AND DATA REDUCTION

We obtained long-slit spectra of the night sky using the Boller & Chivens Spectrograph on the 2.5m duPont Telescope at Las Campanas Observatory (LCO) on the nights of 1995 November 26–29. The first night of the run was lost to clouds. On the third night, a thermal short in the dewar caused poor temperature regulation of the

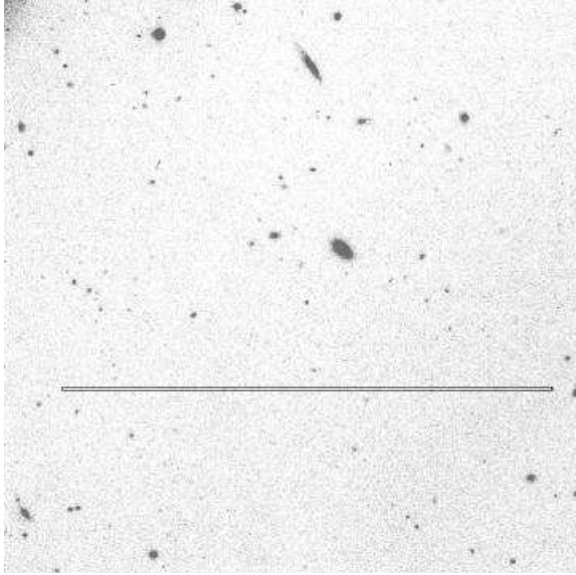


FIG. 2.— The slit position during program observations. The image is a  $4 \times 4$  arcmin $^2$ ,  $r$ -band exposure taken the 2.5m duPont telescope at Las Campanas Observatory. WFPC2/HST observations were taken in parallel with the spectroscopy presented here for the purpose of measuring the EBL. For comparison, the WFPC2/HST field of view is also contained within this image, located towards the lower left quadrant (see Figure 7, Paper I).

CCD which resulted in low and variable charge transfer efficiency (see §3.1). The data from these two nights were therefore dropped from further analysis. The dewar was repaired for the remaining nights of the run. As discussed further in §3.3 and §3.6, both detector performance and photometric conditions were stable to better than 1% on the two useful nights of the run.

As described in Paper I, these spectra were taken within the field of view of our HST/WFPC2 observations, which executed in consecutive orbits on 1995 November 27–28. Because the HST and LCO observations executed simultaneously and along exactly the same pointing (see Paper I), the ZL contribution to both data sets is identical. The slit position is shown overlayed on a  $r$ -band image of the field in Figure 2. The exact coordinates of the spectroscopic observations were selected from ground-based imaging to avoid objects brighter than  $r = 26$  mag arcsec $^{-2}$ . This was done for convenience in the data reduction; extragalactic sources need not be rigorously avoided, as spectral lines from extragalactic sources fainter than  $r \sim 24$  AB mag will be significantly redshifted, on average, and should not align with solar features. In addition, such objects will have low enough surface number density ( $< 0.2$  arcsec $^{-2}$ ) that they will not significantly impact the average extracted spectrum.

We used a 600 l/mm grating to obtain spectra over the wavelength range 3860–5150Å with a dispersion of  $\sim 1.3$ Å per pixel. The wavelength range was chosen to include a maximum number of strong Fraunhofer lines while avoiding strong airglow features. The strong MgI Fraunhofer lines near  $\sim 5170$ Å were identified in an earlier run to be affected by rapidly variable airglow features and were therefore excluded from our 1995 spectral coverage. Ca H & K were included in our observations at the blue end.

A slit-width of  $\sim 1.5$  arcsec (see §3.6.3) produced roughly 2.6Å resolution in the program observations. Even though the ZL has a surface brightness of  $\mu_V \sim 23.2$  mag arcsec $^{-2}$ , we obtained a signal-to-noise ratio of  $\sim 40$  per spectral resolution element from a single, 30 minute exposure by integrating over the total slit surface area ( $\sim 300$  arcsec $^2$ ). To minimize read-noise, we binned the data on-chip by four pixels in the spatial direction and averaged over the full 3.4 arcmin spatial extent of the slit in the data reduction.

Spectrophotometric standards were observed through a slit 10.8 arcsec wide. The detector we used is a thinned Tektronics/SITe CCD with  $1024 \times 1024 \times 24\mu\text{m}$  pixels,  $1.15\text{e}^-/\text{DN}$  gain, and  $8.6\text{e}^-$  read-noise in the  $4 \times 1$  binned configuration. The quantum efficiency of the CCD is near 50% over the spectral range of these observations; however, the spectrograph throughput drops by a factor of two between 5000Å and 3800Å, as can be seen from the sensitivity curve plotted in Figure 5. The upper panel of Figure 3 shows the wavelength calibrated spectrum obtained from one spatial resolution element (1 column) of one of the  $4 \times 1$  binned exposures; the lower panel shows the averaged spectrum from the full image (87 columns). Above 4100Å, the count rate from sky is more than twice the dark rate. The maximum error is 10% per resolution element at the blue end of the spectra, simply due to the low count-rate at bluer wavelengths. Above 4100Å, the error per resolution element is roughly 1%.

Final calibration errors are summarized in Table 1. The data reduction steps are described below in the order which they were performed.

### 3.1. Detector Linearity

Because our observations of the ZL have total count levels in the range 20–50 DN pixel $^{-1}$ , and the standard star observations have close to 5000 DN pixel $^{-1}$ , it is crucial to verify that the CCD is linear over this broad range. In these data, 16 rows are read off beyond the physical extent of the chip, averaged together, and recorded as a bias row, which can be used as an accurate diagnostic of the charge transfer efficiency (CTE) of the CCD. Because the slit only illuminates the central third of the chip, any residual charge which is not passed through the parallel gates (due to low CTE) will appear as a jump in the charge level of the bias row at the boundary between the exposed and unexposed regions of the chip. It is evident from this diagnostic that the temperature regulation of the chip became erratic during the third night of the run, causing an increase in the spurious charge and causing the CTE to drop to an unacceptable level ( $\sim 99.995\%$  per transfer, or 95.0% over 1024 rows). The data from this night were excluded from the analysis because charge shared between rows due to incomplete charge transfer will affect the apparent strength of spectral features. On the nights during which the temperature of the CCD remained stable, the mean level in the bias row was not detectably higher in columns illuminated by the slit than in those which were not illuminated. This was true even for dome flats images, in which the mean level of the illuminated columns was  $\sim 7000$  DN pixel $^{-1}$ . In addition, our final results are based on data imaged in rows 1–700 of the CCD. The data which contribute to our final results were obtained with a min-

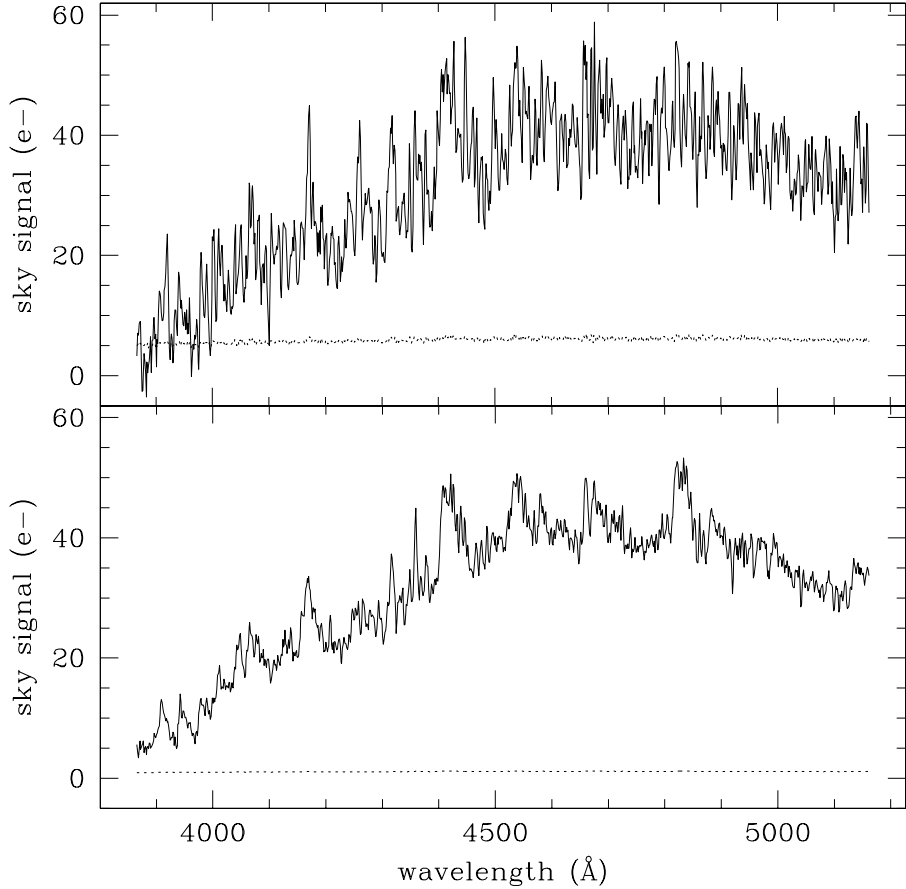


FIG. 3.— Signal-to-noise of program data. The upper plot shows the wavelength-calibrated spectrum in electrons per pixel obtained from one spatial resolution element (column) of an 1800 second exposure of the night sky. The lower plot shows the spectrum produced by averaging 87 columns. The corresponding error spectra, both read-noise dominated, are shown with a dotted line at the bottom of each plot.

imum CTE of 99.9995% per transfer, or 99.7% over 700 rows.

Another possible cause of non-linearity at low count levels is deferred charge. We performed the standard tests for deferred charge as described in Gilliland (1992) and find that only 0.3% of the pixels showed deviations from linearity greater than four times the read-noise. Pixels exhibiting non-linearity were flagged in all images and excluded from analysis. We also performed a standard linearity test by taking dome flat-field exposures with integration times between 0.5 and 200 seconds and looking for variation in the detected count-rate between 20–20,000 DN pixel<sup>-1</sup>. The influence of lamp instability was minimized by taking several series of exposures and averaging the results. The detector response was linear to the limits of the sampled range which more than brackets the signal level of the standard star observations (peaking at roughly 5,000 DN) and the program observations (20–50 DN on average). Non-repeating deviations of less than 1% were attributed to the instability of the lamp.

### 3.2. Bias Subtraction

As discussed in §2 above, we use the strength of the solar Fraunhofer lines in the ZL spectrum to measure the

ZL flux. This is a differential measurement in the dispersion direction; uniform, additive offsets due to bias or dark current will not affect our results beyond the small effect on flux calibration. Structure in either bias or dark current, however, will increase random errors in the results. For example, sharp features in the dispersion direction will increase the *rms* errors in the average strength of the Fraunhofer absorption lines. Also, because we extract a single, one dimensional spectrum from every two dimensional image by averaging over the full spatial extent of the spectrum, any fluctuations in bias level in the spatial direction add random errors to the averaged flux found at any wavelength.

To remove spatial variations in both directions, the bias correction was done in three steps. Variations in the dispersion direction were subtracted using the 150 column overscan region. The overscan was fitted with a Savitsky–Golay routine (Press *et al.* 1992), which follows rapid jumps in the mean level, and the fit was then subtracted from each column. The mean bias level was then removed by subtracting a single mean bias value, which is the average of the bias row (row 1024) in each frame. Finally, bias variations over the chip were found to be very stable after the overscan column and mean bias level were

TABLE 1  
ERROR BUDGET FOR ZODIACAL LIGHT FLUX

Step	Statistical Uncertainty	Systematic Uncertainty
Bias level removal (§3.2)	< 0.01%	...
Dark current removal (§3.3)	< 0.01%	...
Pixel-to-pixel flat-fielding (§3.4)	< 0.01%	...
Slit illumination (§3.4)	...	< 0.1%
Point source flux cal. (§3.6.1)	...	0.6%
Aperture correction (§3.6.2)	...	0.2%
Solid angle (§3.6.3)	...	0.6%
$I_{\text{scat}}(\text{ZL})$ estimate (§A.2)	...	1.2%
$I_{\text{scat}}(\text{ISL})$ estimate (§A.3)	...	0.5%
<i>rms</i> scatter in ZL correlation (§5,§6)	0.6%	...
Combined ( $1\sigma$ ) <sup>a</sup>	0.6%	1.1%

<sup>a</sup>Statistical errors have been combined in quadrature to obtain a cumulative, one-sigma error. Systematic errors have been combined assuming a flat probability distribution for each contributing source of error. The resulting systematic error is roughly Gaussian distributed, and the quoted value is the 68% confidence interval. For a detailed discussion see Paper I.

subtracted from every image. These variations were thus removed by subtracting a “superbias” image, which is the average of 250, overscan- and bias-subtracted bias frames. To verify the accuracy of this procedure, we test-reduced 50 bias frames which had not been included in the superbias. After bias subtraction, these test frames had an average value of 0.005 DN with an *rms* scatter of 0.03 DN and no residual systematic structure.

### 3.3. Dark Current Subtraction

Dark frames were taken immediately before and after observations on each night, and 20 darks were taken at the start and end of the run, which were combined to make a “superdark,” the mean level of which drifted by  $\sim 1.0$  DN over the extent of the frame. Unfortunately, the 20-frame superdark is read-noise dominated and cannot provide a pixel-to-pixel correction. The superdark was therefore smoothed using a sliding  $3 \times 3$  boxcar median filter, in order to avoid adding noise and to allow the removal of the mean dark level. The frames taken during the run were used to test the accuracy of the superdark: after bias subtraction (as described above) and dark subtraction, the test-reduced darks taken at the beginning and end of the observations on 1995 November 27 and 29 had a mean level of  $\pm 0.25$  DN with no coherent pattern.

### 3.4. Flat Fielding and Illumination Correction

We used a 1.5 arcsec slit for the program observations in order to preserve resolution. However, we used a 10.8 arcsec slit for the standard star observations in order to collect as much light as possible. Different sets of flat-field and illumination corrections were therefore required for two reasons. First, microscopic roughness on the edges of the slit jaws caused shadowing which changed as a function of slit-width. Second, the slit-jaw mechanism on this spectrograph is such that the jaws are parallel for separations up to  $\sim 5.4$  arcsec (500 $\mu$ m) but are not parallel when the jaws are set to 10.8 arcsec in the center. Variation in slit-width is almost 10% from end-to-end when the width at the center is 10.8 arcsec. To compensate for the vari-

able slit-width for standards, the illumination corrections for both slit-widths were normalized to the spatial center of the slit. Standard stars were all observed within two pixels of the central column used for normalization, which places them within 99.98% of the nominal value for the wide-slit illumination correction. Flat-field and slit-illumination corrections were created from dome and twilight sky flats, respectively, using the tasks RESPONSE and ILLUMINATION in the IRAF SPECRED package.

### 3.5. Wavelength Calibration

Wavelength solutions were based on He-Ar comparison spectra taken before and after each 1800 second program exposure and immediately after each standard star observation. At the beginning of the run, great care was taken to align the dispersion axis with the pixel rows: the *rms* variation in the centroid position of arc lines over the full 3.4 arcmin spatial extent of the images is typically 0.05 – 0.12 pixels. This is true over the full wavelength range. Consequently, it was not necessary to rectify the two-dimensional program spectra of the zodiacal light (night sky). Each program spectrum was simply averaged along rows (with  $5\sigma$  cosmic ray rejection) to obtain a one-dimensional spectrum, and a wavelength solution based on the spatial center of the image was applied afterward. Standard stars were first extracted to produce one-dimensional spectra and then wavelength calibrated in the usual way.

We identified 21–25 features in each comparison spectrum visually and fitted a third order (four term) Legendre polynomial to the pixel-wavelength solution to obtain a dispersion curve. This was done using the IDENTIFY task in IRAF. The *rms* residuals in the wavelength solution were 0.016–0.04 $\text{\AA}$ . Shifts in the wavelength solution between program observations were less than  $\pm 1.5$  pixels from the start to the end of the night. Linear dispersion solutions were applied using the task DISPCOR.

### 3.6. Flux Calibration

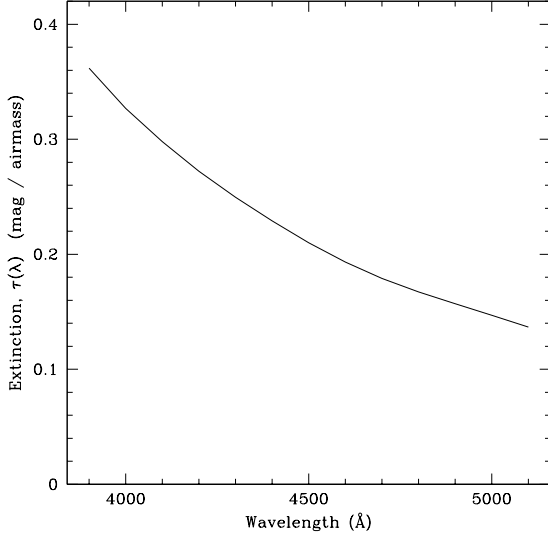


FIG. 4.— The extinction function derived from observations of standard stars taken on 1995 November 27 and 29. Extinction solutions for the two nights individually were found to be identical to within the one-sigma statistical errors ( $\lesssim 0.01$  mag). The function shown is a sixth-order Legendre polynomial fit to extinction coefficients obtained in 50Å wide bins.

Three independent components of the surface brightness calibration will affect its final accuracy: point source calibration (which includes the sensitivity and extinction corrections); aperture correction (which compensates for the loss of light from point source observations which does not occur in observation of a uniform aperture-filling source); and the fiducial standard star system. The flux calibrated spectrum for a uniform source can be expressed as

$$I(\lambda) = \frac{C(\lambda) S(\lambda) T(A) 10^{0.4\chi\tau(\lambda)}}{\Omega}, \quad (2)$$

in which  $C(\lambda)$ , is the wavelength calibrated spectrum in  $\text{DN sec}^{-1}\text{Å}^{-1}$  per pixel,  $S(\lambda)$  is the sensitivity function in  $\text{ergs DN}^{-1}$ ,  $T(A)$  is the aperture correction for the slit size in question,  $\chi$  is the airmass of the observation,  $\tau(\lambda)$  is the extinction correction expressed in  $\text{mag airmass}^{-1}$ , and  $\Omega$  is the solid angle of each pixel in steradians per pixel. We discuss each component of the calibration separately below.

### 3.6.1. Point Source Calibration

We observed Hamuy *et al.* (1992, hereafter H92) tertiary spectrophotometric standards roughly 15 times each night. For each standard observation, we first centered the star in a narrow slit ( $\sim 2$  arcsec), and opened the slit to 10.8 arcsec after guiding was established. Nine different standards were observed throughout the run, with colors  $0.0 < (B - V) < 0.6$  mag. This range represents as broad a distribution as is available from the H92 standards and does bracket the color of the night sky. All standards were observed with the slit aligned along the parallactic angle (Filippenko 1982).

One-dimensional spectra were extracted from the two-dimensional images and wavelength calibrated in the usual

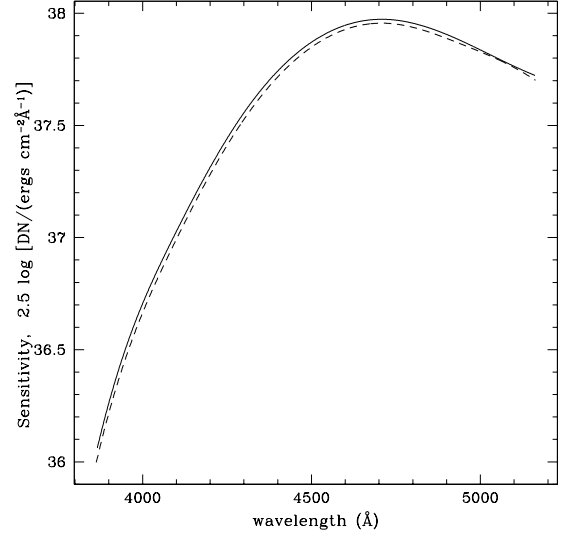


FIG. 5.— Two sensitivity functions obtained from observations of tertiary standards on different nights. The solutions differ by 1-2%, well within the fluctuations expected to arise from small temperature variations of the CCD.

way using the APSUM and DISPCOR tasks in IRAF. Extinction corrections were calculated from standard star observations themselves in 50Å bins for each night individually. Typical residuals in the extinction solution in each 50Å bin were 0.009 mag (*rms*) in the data taken on 1995 November 27 and 29. As no difference was found between the two nights, the final extinction solution was constructed from the data taken on both nights together using a sixth-order Legendre polynomial fit to the extinction as function of wavelength (see Figure 4), with an uncertainty of 0.2% as a function of wavelength. The resulting extinction curve is in excellent agreement with the *r*- and *g*-band extinction terms which we obtained from images taken simultaneously with the 1m Swope telescope at the same site.

After the extinction corrections were applied to the standard star spectra, the sensitivity curve for each night was determined using the task SENSFUNC in the IRAF SPCRED package. The agreement between the sensitivity curves for the two nights is excellent: the variations between the sensitivity curves found for 1995 November 27 and 29 are 3% at 4100Å, and 2% red-ward of 4500Å (see Figure 5). Variations in the quantum efficiency of the CCD on this level are expected to result from temperature changes of a few degrees (M. Blouk, personal communication), so we do allow the sensitivity function solutions to be slightly different from night to night. The standard deviation in the SENSFUNC solution for both nights is 0.011 mag, which translates into a 0.3% error in the mean sensitivity as a function of wavelength from 15 standard star observations. To be conservative, we adopt a systematic uncertainty in the point source calibration of 0.6%. Systematic errors in the tertiary standard star system of Hamuy *et al.* are discussed in §3.7. They are not included in the accuracy of the zodiacal light measurement discussed here. Those uncertainties are, however, relevant

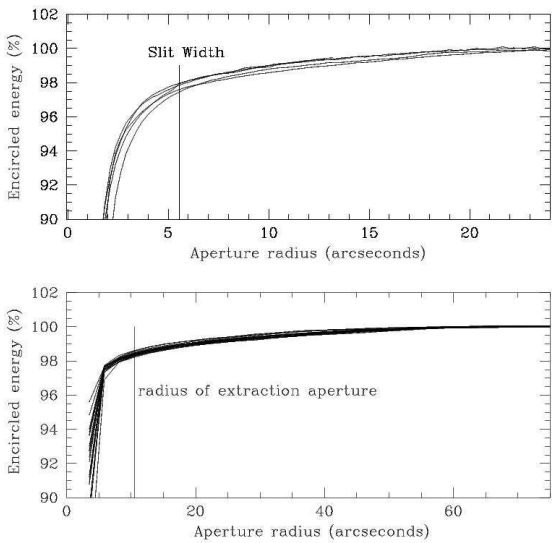


FIG. 6.— The upper plot shows encircled energy curves for stars imaged directly in the focal plane of the du Pont 2.5m telescope. The half-width of the slit (5.8 arcsec) used for standard star observations is indicated by the solid vertical line. The percentage flux from a point source which passes through this aperture is  $97.9 (\pm 0.2)\%$ . The lower plot shows the encircled energy curve along the spatial extent of a spectroscopic image, showing that  $98.4 (\pm 0.1)\%$  of the light entering the spectrograph from a point source is recovered when a  $\pm 10$  arcsec extraction aperture is used.

to the EBL detection for which we have used this zodiacal light measurement. That error is explicitly included in final accuracy of the EBL detections discussed in Paper I.

### 3.6.2. Aperture Correction

The aperture correction compensates for flux which is lost from the point source observations in two distinct ways. First, light is lost in the focal plane of the telescope if the radius of 100% encircled energy is larger than the half-width of the slit. Second, when a one dimensional spectrum is extracted from the two dimensional, dispersed image, some light will lie outside the extraction aperture in the spatial direction.

To measure flux lost in the aperture plane, we measured the PSF from images taken on the last night of the run (1995 November 30). We plot the encircled flux with radius (growth curve) for five stars in Figure 6. To be certain that focus does not affect the PSF at a 5 arcsec radius, the stars used for this plot were taken with widely varying focus. As 5 arcsec in the focal plane of the duPont 2.5m Telescope corresponds to 0.45 mm (almost 19 pixels) it is difficult to have the telescope out of focus enough to affect the enclosed flux at a radius of 5 arcsec. This is clear from the lack of variation in the shape of the growth curves shown in the figure. The fractional flux enclosed by the half-width of the slit used for standard star observations is  $0.979 (\pm 0.002)$ .

To determine the percentage flux lost once through the slit, we have mapped the growth curves along the spatial extent of the two dimensional spectra for all 45 standards taken during the run. The sky level for this test was taken from pixels further than 80 arcsec from the peak of the

star. We averaged 400 rows near the peak sensitivity of the spectrograph to increase the signal-to-noise. To confirm that the PSF has negligible wavelength dependence, we calculated the aperture correction at both the blue and red ends of the spectral range and found no variation in the growth curve. The growth curve along the slit for the 18 highest signal-to-noise spectra are shown in Figure 6. The differences in the encircled energy at the inner-most radii plotted are a result of differences in sub-pixel centering for spectra observed with  $4 \times 1$  binning. This does not affect our results for spectra extracted to an aperture of  $\pm 4$  (binned) pixels ( $\pm 10.6$  arcsec). As this plot shows, the extraction aperture is well within the region of good signal-to-noise in the star, and includes  $98.4 (\pm 0.1)\%$  of the flux from a point source which passed through the spectrograph slit. Sky background was measured outside an annulus of 25 pixels (60 arcsec) from the peak of the star. This aperture is small enough to ensure adequate signal-to-noise in the extracted stellar spectrum, and also ensures minimal error due to sky subtraction, as the stellar signal is much brighter than the sky background in the inner 10.6 arcsec.

The total aperture correction for a uniform surface brightness, aperture-filling source is then the fractional flux recovered for a point source, or  $T = 0.963 (\pm 0.002)$ .

### 3.6.3. Solid Angle of the Program Observations

The solid angle is a function of both the angular pixel scale (spatial direction) and the angular slit-width (dispersion direction). The pixel scale was measured empirically by taking spectra of two stars with known angular separation while they were simultaneously aligned in the slit. The measured separation in pixels was then compared to the known angular separation of the stars. Four pairs of stars were observed in this way with angular separations in the range 44–82 arcsec. Each pair of stars was observed with the slit at 3 positions differing by less than 1 degree, in an attempt to obtain truly parallel slit alignment. The stars used for this purpose are in the field of M67, for which the relative astrometry of members is known to better than 0.3 mas (Girard *et al.* 1989). The pixel scale was found to be  $0.5843 \pm 0.0035$  arcsec pixel $^{-1}$  ( $1\sigma$  error).

The slit-width of the spectrograph is adjusted by a manual micrometer while the instrument is on the telescope. The calibration and repeatability of the micrometer was verified using a microscope. The repeatability of the width setting was tested by opening the jaws to their maximum extent between each of several sets of measurements. At the micrometer setting used for our program observations, the slit width was measured to be  $1.536 \pm 0.002$  arcsec ( $1\sigma$  error) at the center of the jaws. The total solid angle of each pixel is therefore  $0.8975 \pm 0.0054$  arcsec $^2$  ( $1\sigma$  error).

### 3.7. Accuracy of Tertiary Standards

Hamuy *et al.* (1992) quote the internal precision of their tertiary spectrophotometric system to be better than 0.01 mag at all wavelengths, a claim which is well corroborated by the small statistical errors we find in our own spectrophotometric flux calibration (see below). An additional concern for our purposes, however, is the agreement between the H92 system and the primary calibration for Vega in the spectral range of our observations (approximately the Cousins  $B$ -band, 4200–5100Å).

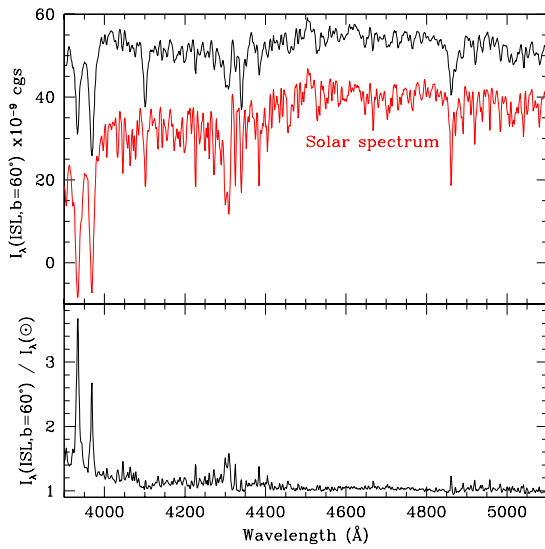


FIG. 7.— In the upper plot, the spectrum of the integrated starlight (ISL) at  $|b| = 60^\circ$  is compared to the solar spectrum, which has been scaled to the same flux and offset to allow visual comparison of the spectral features. The lower plot shows the ratio of the two, normalized at 4600Å. Both plots show visually and quantitatively that the absorption lines in the ISL spectrum are weaker than the same features in the solar (and therefore zodiacal light) spectrum.

The tertiary system of H92 is calibrated based on the equatorial secondary standards of Taylor (1984), which is in turn calibrated to the primary calibration of Vega by Hayes & Latham (1975). As described in H92, they recalibrate the Taylor (1984) secondary standards to the now widely-accepted Hayes (1985, hereafter H85) calibration of Vega. Details of that process are documented in H92. H92 estimate that their internal consistency in converting Taylor (1984) to the Hayes (1985) Vega system is 0.009 mag in the wavelength range of the Cousins  $B$ . They also compare synthetic photometry of the adjusted Vega spectrum with Johnson & Harris (1954) photometry of Vega and find an offset of  $-0.016 (\pm 0.009)$  mag at  $B$  (in the sense of Taylor minus Johnson). This offset seems to be intrinsic to the Vega calibration, as Hayes also finds that offset between his observations of Vega and the original Johnson observations. We therefore conclude that the statistical accuracy of the tertiary system is roughly 1% and the systematic uncertainty is roughly 1.5%.

#### 4. COMPONENTS OF THE NIGHT SKY SPECTRUM

The spectrum of the night sky from Earth includes integrated starlight (ISL), zodiacal light (ZL), EBL, and diffuse Galactic light (DGL) from above the atmosphere, as well as atmospheric emission, or airglow. Light from all sources is scattered by molecules and particulates in the atmosphere, causing considerable redirection from one line of sight to another. Absorption by particulates is a minor effect compared to the scattering by both components. The net effect of atmospheric scattering on a source with small angular extent (e.g. stars and galaxies) is atmospheric “extinction.” The net scattering out of the line of sight can be measured in the typical way using standard stars, as in §3.6. Light from a very extended source (e.g. ZL,

ISL) will not suffer the same “extinction”; rather, it will appear to be smoothed out over the sky as light from different regions scatters into and out of the line of sight. The efficiency of scattering in the atmosphere is conveniently described in the familiar way as the extinction along the line of sight  $\tau_{\text{obs}}(\lambda)$ .

If the scattering angles were small, and the diffuse, extended source were uniform over the sky, then the scattering into and out of the line of sight would roughly cancel. However, Rayleigh scattering occurs over very broad angles and the relative surface brightness of ZL and ISL changes strongly over the sky. We must therefore explicitly calculate the net effects of scattering in our observing situation (determined by the observatory location and positions of the Sun, Galaxy, and target), as they are not intuitive. This is done in detail in the Appendix. We summarize the results here.

We can describe the observed spectrum of the night sky in the target field,  $I_{\text{NS}}$ , as follows:

$$I_{\text{NS}}(\lambda, t, \chi) = I_{(3h, -20d)}(\lambda) e^{-\tau_{\text{obs}}(\lambda)\chi} + I_{\text{scat}}(\lambda, t, \chi) + I_{\text{air}}(\lambda, t, \chi), \quad (3)$$

in which  $I_{(3h, -20d)}(\lambda)$  is the flux from the target field (coordinates  $\alpha = 3.00h$ ,  $\delta = -20.18d$ ),  $\tau_{\text{obs}}(\lambda)$  is the extinction for a point source,  $\chi$  is the airmass of the target field at the time of observations,  $I_{\text{scat}}(\lambda, t, \chi)$  is the light scattered into the line of sight as a function of time and wavelength, and  $I_{\text{air}}(\lambda, t, \chi)$  is the effective airglow along the line of sight (including any scattering effects which redistribute airglow over the sky). The flux from the target field,  $I_{(3h, -20d)}(\lambda)$ , includes the EBL, DGL and ZL flux within the solid angle of the slit. There is no ISL component coming directly from the target field because the slit simply contains no stars to  $V = 24$  mag. The slit also provides an extremely effective pupil stop which prevents contributions from discrete sources off-axis.<sup>1</sup>  $I_{\text{scat}}(\lambda, t, \chi)$  can be expressed as

$$I_{\text{scat}}(\lambda, t, \chi) = I_{\text{scat}}^{\text{R}}(\lambda, t, \chi, \text{ZL}) + I_{\text{scat}}^{\text{M}}(\lambda, t, \chi, \text{ZL}) + I_{\text{scat}}^{\text{R}}(\lambda, t, \chi, \text{ISL}) + I_{\text{scat}}^{\text{M}}(\lambda, t, \chi, \text{ISL}) \quad (4)$$

where the superscript R or M denotes Rayleigh scattering (due to molecules) or Mie scattering (due to particulates), the parenthetical ZL or ISL denotes the source being scattered, and the parenthetical  $\lambda$ ,  $t$ , and  $\chi$  denote dependence on those variables. We do not include the DGL in Equation 4 explicitly because the total DGL is at least a factor of 50 times fainter than the direct ISL and is therefore a trivial component ( $< 0.2\%$  at  $2 < \text{UT} < 6.5$ ) of the scattered light. The EBL is not included as it does not have strong spectral features (see §5).

At any altitude, Rayleigh scattering is the dominant effect. Because the particulate density is concentrated at low altitudes, this is especially true at high altitude observatories. The total extinction, as measured for a point source,

<sup>1</sup>No stars with  $V < 12$  mag are within 12 arcmin of the slit, and no stars with  $V < 7$  are within 1.5 degrees. We have carefully characterized the scattered light properties of the duPont telescope by positioning a  $V = 4$  mag star around the field from on-axis to 20 arcmin off-axis in 4 directions at 1 arcmin intervals. The stray light entering the slit from discrete off-axis sources is more than  $10^{-6}$  fainter than surface brightness of the ZL in the field. See Paper I for further discussion.

is equal to the sum of the molecular and particulate extinction,  $\tau_{\text{obs}}(\lambda) = \tau_{\text{M}}(\lambda) + \tau_{\text{R}}(\lambda)$ . Rayleigh extinction,  $\tau_{\text{R}}$ , can be calculated from the well-known density distribution of the atmosphere for any observatory. Mie extinction, which varies with time and geography, can be inferred from the difference between the observed and Rayleigh extinction. At LCO, the extinction due to Mie scattering is 20–40% of the Rayleigh extinction.

We have calculated the scattered light from all terms in Equation 4 in the Appendix at 30 minute intervals throughout the nights of our observations. To briefly summarize the results of our calculations, the ZL total flux scattered into the line of sight (*gained*) at any time during our observations is less than the total flux scattered out of the line of sight (*lost*). Thus, the net result of atmospheric scattering for the case of ZL in our situation is still a net *extinction* of order 2–8%, which we can conveniently describe by an effective extinction,  $\tau_{\text{eff}}$ , which we use in place of  $\tau_{\text{obs}}$  for ZL (see Figures A10 and A11 in the Appendix). We can check the scattering predictions of our calculations in our ZL analysis itself by looking for changes in the ZL solution with time. We estimate that our calculation of the scattered ZL has an average uncertainty of 8%, which translates into a systematic uncertainty in our ZL measurement of 1.2%.

In the case of the ISL, the total flux gained due to scattering into the line of sight is 12–24% of the total ZL flux from low to high airmass. However, the crucial issue is not the total mean flux, but rather the strength of the spectral features which are in common with the Sun (see Figure A15 in the Appendix). The net influence of the scattered ISL on observations is to increase the strength of the Fraunhofer lines over the night by 0.6–4% redward of 4100Å, and 5–35% blueward. Because the effect is a strong function of wavelength, it is straightforward to identify inconsistencies between the predicted ISL flux and our observations by looking for changes in the ZL solution with wavelength. We estimate that our calculation of the scattered ISL has an uncertainty of 13%, which translates into a systematic uncertainty in our ZL measurement of 0.5% over the majority of our wavelength range.

## 5. ANALYSIS

Based on the discussion in the previous section, we can characterize the observed spectrum of the night sky,  $I_{\text{NS}}$ , at any time as a combination of airglow, zodiacal light (ZL), diffuse Galactic light (DGL), and scattered interstellar light (ISL) as follows:

$$I_{\text{NS}}(\lambda, t, \chi) = I_{\text{air}}(\lambda, t, \chi) + I_{\text{scat}}(\lambda, t, \chi, \text{ISL}) + I_{\text{ZL}}(\lambda) e^{-\tau_{\text{eff}}(\lambda, t)\chi} + [I_{\text{EBL}}(\lambda) + I_{\text{DGL}}(\lambda)] e^{-\tau_{\text{obs}}(\lambda)\chi}, \quad (5)$$

in which  $\tau_{\text{eff}}(\lambda, t)$  is now the effective extinction for ZL discussed in §4 and  $I_{\text{scat}}(\lambda, t, \chi, \text{ISL})$  is the total scattered ISL flux due to Rayleigh and Mie scattering in the atmosphere.

Sharp spectral features are not expected in the EBL because redshifting will blur any distinct spectral features. The EBL will therefore not affect our measurements of the ZL from the strength of the observed Fraunhofer lines. The diffuse Galactic light, which results from scattering of the ambient interstellar radiation field by interstellar dust,

is very weak in our field (0.8% of the ZL flux, see Paper I). In addition, as we have already discussed regarding the scattered ISL, the strength of the spectral features we use in our analysis is roughly 1.5 to 3.8 times weaker in the DGL than in the ZL spectrum. The DGL from the target field thus contributes at most 0.2–0.5% percent to the final result (see Figure 7). We subtract this contribution from our ZL measurement after the fact at a level of 0.3%. Emission lines due to ionized gas in the DGL do not contribute in the spectral range of these observations (see Paper I, Martin *et al.* 1991, Dube *et al.* 1979, and Reynolds 1990).

The observed spectrum can therefore be expressed as the sum of four components: (a) an unstable emission line spectrum, due to airglow; (b) a stable and featureless component, due to EBL; and (c) a stable, absorption line component, due to ZL; and (d) a time variable absorption component due to scattered ISL. The component (c) can be ignored, and (d) has been calculated. The portion of the night sky spectrum which has variable spectral features can therefore be expressed as

$$I_{\text{obs}}(\lambda, t, \chi) = I_{\text{air}}(\lambda, t, \chi) + I_{\text{scat}}(\lambda, t, \chi, \text{ISL}) + c(\lambda) I_{\odot}(\lambda) e^{-\tau_{\text{eff}}(\lambda, t)\chi}, \quad (6)$$

in which  $I_{\odot}(\lambda)$  is the solar spectrum and  $c(\lambda)$  is a scaling factor which relates the mean surface brightness of the ZL to the mean flux of the Sun.

Identifying the appropriate scaling spectrum,  $c(\lambda)$ , is complicated by the fact that the ZL — a pure absorption line spectrum — is greatly obscured by the emission line spectrum of the airglow in the night sky. Airglow features do overlap with some of the solar Fraunhofer lines, as can be seen in the comparison of a night sky spectrum and a scaled solar spectrum shown in Figure 8. The strength of particular airglow lines can vary by several percent during a single night, as can be seen in the comparison of two night sky spectra shown in Figure 9. The airglow spectrum is composed of an effective continuum due to O+NO (NO<sub>2</sub>) recombination, broad rotation–vibration transition bands, scattered light, and blended lines, making a continuum level impossible to identify. Not only do rapid temporal variations occur with (de)ionization, but airglow is also a complex function of airmass, observatory location, and local atmospheric conditions such as volcanic activity (van Rhijn 1924, 1925; Roach & Meinel 1955). In short, a stable, fiducial airglow spectrum with meaningful absolute or relative flux cannot be defined. As a result, it is not possible to measure the equivalent width of individual ZL Fraunhofer lines because the ZL continuum level is well hidden. Instead, we have developed a conceptually simple approach to the problem of determining the scaling factors  $c(\lambda)$  which does not involve measuring the equivalent widths explicitly.

We begin with the assumption that the intrinsic airglow spectrum, time- and airmass-dependent though it may be, does not have spectral features in common with the ZL spectrum. This is borne out by the fact that we get consistent solutions using eight distinct spectral regions spread over 1100Å (see §5). When we subtract  $I_{\text{scat}}(\lambda, t, \chi, \text{ISL})$  and scaled solar spectrum with the correct value for  $c(\lambda)$ , what remains is a pure airglow spectrum, free of solar features:

$$I_{\text{air}}(\lambda, t, \chi) = I_{\text{obs}}(\lambda, t, \chi) - I_{\text{scat}}(\lambda, t, \chi, \text{ISL})$$

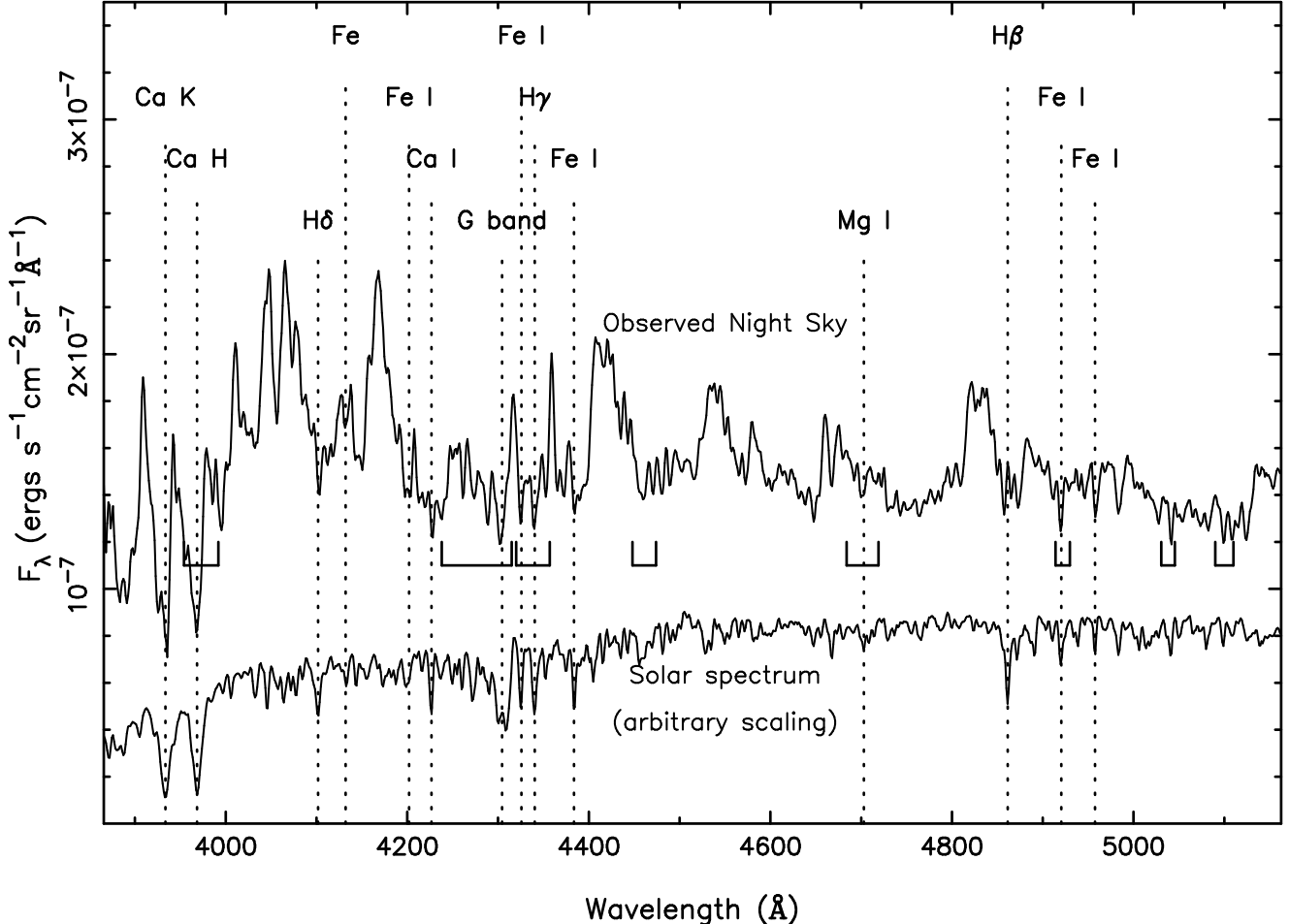


FIG. 8.— The observed spectrum of the night sky compared to a solar spectrum at arbitrary absolute flux. The solar Fraunhofer absorption lines which are preserved in the ZL are clearly visible in the spectrum of the night sky. The strongest of these lines are marked; several blended solar features are also seen in the night sky spectrum. Square brackets indicate the wavelength regions used in the final analysis.

$$-c(\lambda)I_{\odot}(\lambda)e^{-\tau_{\text{eff}}(\lambda,t)\chi}. \quad (7)$$

We use a linear correlation function to determine when the difference (residual airglow) spectrum is uncorrelated with the solar spectrum and is consequently free of solar features. When the correlation between the difference spectrum and solar spectrum is minimized, the correct ZL surface brightness has been subtracted from the observed night sky.

The only available, high-resolution spectrum of the Sun is the National Solar Observatory Solar Flux Atlas of the integrated solar disk at 0.01Å resolution. The statistical error in the flux calibration of this spectrum is 0.25% as estimated by agreement in overlapping sections of the normalized spectrum. The effects of atmospheric absorption by H<sub>2</sub>O or O<sub>2</sub> are negligible below 6500Å, as described in the published Atlas (Kurucz *et al.* 1984). In the optical, the normalized spectrum can be converted to absolute solar irradiance using the Neckel & Labs (1984) (NL84) absolute calibration. As the NL84 is the standard with respect to which the ZL color is defined, the absolute accuracy of the fiducial solar spectrum is not a source of error in this work. The Solar Flux Atlas, calibrated to NL84, was obtained in digitized form from R.L. Kurucz. It was convolved with a variable width Gaussian to match the

resolution of the observed spectra as a function of wavelength. The wavelength-dependent resolution of each program spectrum was determined from the arc lamp spectra which were used for wavelength calibration.

The execution of this method is complicated by the fact that the relative color of the airglow and solar spectra will dominate the strength of the diagnostic correlation if the continuum shapes of both spectra are not properly removed. In order for the strength of the linear correlation of  $I_{\text{air}}(\lambda)$  and  $I_{\odot}(\lambda)$  to reflect the strength of coincident spectral features, both spectra must have stationary mean values as a function of wavelength, as can be seen clearly in the generic expression for a linear correlation:

$$R(x, y) = \frac{\sum_n (x_n - \bar{x})(y_n - \bar{y})}{\sqrt{\sum_n (x_n - \bar{x})^2} \sqrt{\sum_n (y_n - \bar{y})^2}}. \quad (8)$$

In this case,  $x$  and  $y$  are  $I_{\text{air}}(\lambda)$  and  $I_{\odot}(\lambda)$  respectively, the subscript  $n$  runs over wavelength. It is clear from this expression that the mean flux drops out of the correlation, while differences from the mean are crucial.

Of the 47 strongest solar features, we find that 39 give ZL solutions which vary with time by more than 18% over the night. In all cases, this variation is correlated with the

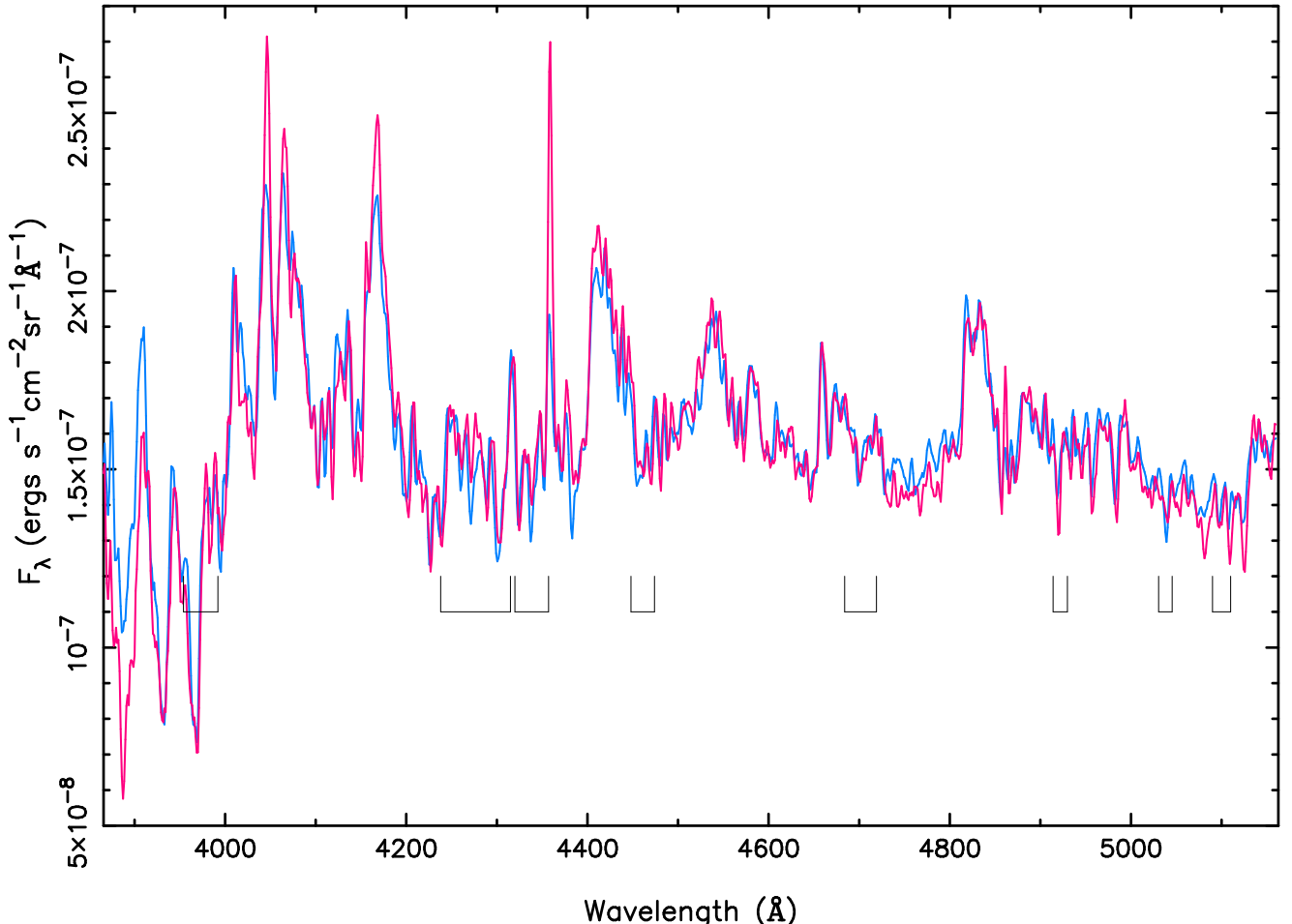


FIG. 9.— Two spectra of the night sky taken on the same night, several hours from twilight. Rapid fluctuations are evident in the strength of many of the airglow features.

strength of adjacent airglow lines. The remaining eight solar features vary by less than 10% with time. The results discussed below are based on these eight spectral regions, indicated in Figures 8 and 9. In these regions, the continuum can be well approximated by a simple second order polynomial fit and easily subtracted, however our results are quite insensitive to the method of continuum fitting. Boxcar smoothing with scales between 75Å and 199Å (at least twice the width of the widest spectral region used in the analysis), second or third order polynomial fitting, and Savitsky–Golay smoothing (Press *et al.* 1992) all produce identical results.

## 6. RESULTS

In Figure 10, we show an example of the correlation strength,  $R$ , and correlation probability,  $P$ , between a ZL spectrum and the spectra which result when we assume a range of values ( $8 \times 10^{-8}$  to  $1.4 \times 10^{-7}$   $\text{ergs s}^{-1} \text{cm}^{-2} \text{sr}^{-1} \text{Å}^{-1}$ ) for the mean ZL flux contributing to one region of one observed night sky spectrum. Where  $R$  and  $P$  go to zero, the correct ZL surface brightness has been removed from the observed night sky spectrum.

The absolute flux of the ZL as measured from each of the 16 spectra taken on 1995 November 27 and 29 are shown in Figures 11–13. In Figure 11, we show the av-

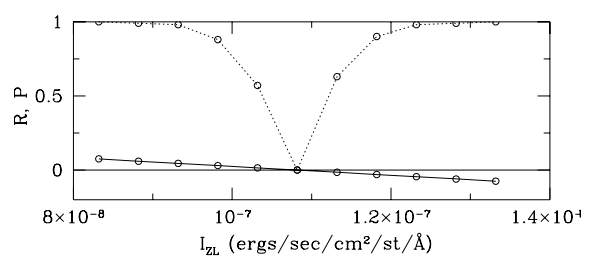


FIG. 10.— The value of the correlation parameters used to define the strength of the correlation between the residual “airglow” spectrum (the zodiacal light-subtracted night sky spectrum) and the ZL spectrum for different assumed contributions of ZL. The points connected by the dotted line indicate the probability that the two spectra are from the same parent set as a function of the ZL flux assumed. The points connected by the solid line indicate the correlation strength, zero being no correlation. These parameters describe a simple linear correlation as defined in equation 8 (see Press *et al.* 1992). The ZL surface brightness identified by this method for the observation shown here is  $1.08 \times 10^{-7}$   $\text{ergs s}^{-1} \text{cm}^{-2} \text{sr}^{-1} \text{Å}^{-1}$ .

erage  $c(\lambda)$  as determined for all 16 spectra over the run for each of the eight spectral regions. The results are normalized to 1.0 at 4650Å. This plot illustrates two points:

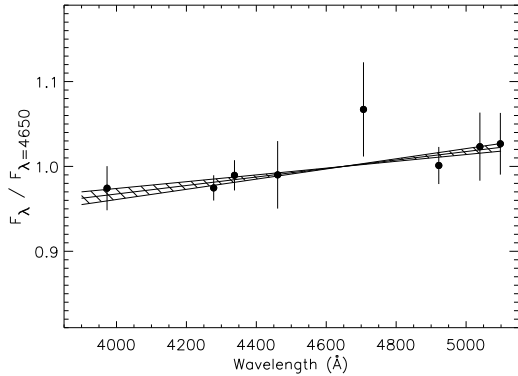


FIG. 11.— The points show  $c(\lambda)$  for the eight spectral regions indicated in Figure 8 as measured from 16 spectra taken on 1995 November 27 and 29, normalized to 1.0 at 4600–4700Å. The error bar on each point indicates the standard deviation in the 16 measurements. The hatched region shows the color of the ZL relative to the solar spectrum determined by a linear least squares fit to the points, excluding the point at  $\sim 4700\text{Å}$ . The best fit color is  $C(3900, 5100) = 1.05 \pm 0.01$ , where the error corresponds to the one-sigma error in the fitted slope. The mean flux of the ZL at 4600–4700Å from this fit is  $109.1(\pm 0.5) \times 10^{-9} \text{ ergs s}^{-1} \text{ cm}^{-2} \text{ sr}^{-1} \text{ Å}^{-1}$ .

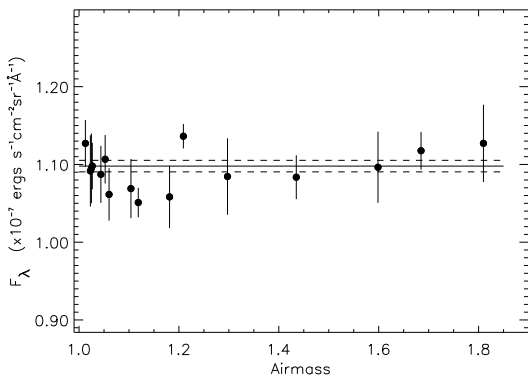


FIG. 12.— The mean value of the ZL at 4600–4700Å as measured in each of the 16 spectra taken on 1995 November 27 and 29, adopting  $C(3900, 5100) = 1.05$ . Each point represents the average of the ZL flux measured in all 8 spectral features in a single observation. The horizontal line shows the mean ZL flux, which is  $109.7(\pm 0.7) \times 10^{-9} \text{ ergs s}^{-1} \text{ cm}^{-2} \text{ sr}^{-1} \text{ Å}^{-1}$ . Dashed lines show the one-sigma statistical error in the mean (0.6%).

(1) from any single spectral feature, we find a solution for the ZL flux with a standard deviation of only 1–6% over 16 individual observations taken on two nights and independently reduced; and (2), the solution from independent spectral features are in excellent agreement, and indicate that the ZL is roughly  $5 \pm 1\%$  redder than the solar spectrum, or  $C(3900, 5100) = 1.05 \pm 1$  (excluding the point at  $\sim 4700\text{Å}$ ). This color is in excellent agreement with previous estimates from the ground and space (see Leinert 1998). It is also in excellent agreement with our own measurement of the ZL color from our simultaneous HST/FOS observations, which give  $C(4000, 7000) = 1.044 \pm 1$  (see Paper I).

From the solution for the ZL as a function of wave-

length we can explore the impact of the scattered ISL flux on our measurements. If we increase (decrease) the total flux of the predicted scattered ISL,  $I_{\text{scat}}(\lambda, t, \chi, \text{ISL})$ , the solution for the ZL decreases (increases) *linearly* in response; a change of 50% in the ISL flux corresponds to a change of 6% in the ZL solution at  $\sim 3950\text{Å}$ , but  $< 2\%$  at the other wavelengths. Thus, increasing or decreasing  $I_{\text{scat}}(\lambda, t, \chi, \text{ISL})$  by 50% makes the ZL solution at  $3950\text{Å}$  inconsistent at the two-sigma level with solutions over the rest of the spectrum for a ZL color of  $5 \pm 1\%$ . Also, increasing or decreasing the ISL flux consistently increases the scatter in the ZL solution at all wavelengths; at  $3950\text{Å}$ , the scatter increases by 40% in response to a change of 50% in the ISL flux at all airmasses. Although this does not allow us to place a stronger constraint on the error in  $I_{\text{scat}}(\lambda, t, \chi, \text{ISL})$  than those discussed in the Appendix, it does provide independent verification that the predicted  $I_{\text{scat}}(\lambda, t, \chi, \text{ISL})$  values are in the right range. It also emphasizes that an error of 10% in  $I_{\text{scat}}(\lambda, t, \chi, \text{ISL})$  changes the mean ZL solution by only 0.4% at 4200–5100Å. As discussed in the Appendix, the uncertainty in  $I_{\text{scat}}(\lambda, t, \chi, \text{ISL})$  contributes an uncertainty to the ZL measurement in §6 of  $< 0.5\%$  (see Table 1).

In Figures 12 and 13 we show the mean ZL solution at 4600–4700Å (for  $C(3900, 5100) = 1.05$ ) as a function of airmass from each of the 16 exposures. Figure 12 shows the solution obtained using all eight spectral features solutions plotted in Figure 11, while Figure 13 shows the solution based on the four spectral features with the smallest standard deviations in Figure 11. The horizontal line in each plot shows the mean, the dashed lines show the one-sigma error in the mean. The difference between the results in the two plots is less than 0.2%. No obvious trends appear in either plot as a function of airmass. In fact, the mean value for points above and below 1.2 airmasses in Figure 13 agrees to better than 0.3% (half of the error in the mean). The error bars in Figure 13 vary from 1–8%, indicative of the small number of measurements (four spectral features) being averaged together to produce the result at each airmass. The standard deviations indicated by the error bars in Figure 12 show less variation from point to point (1.5–5%), as eight measurements contribute to each point.

As discussed in the Appendix, we estimate that the uncertainty in the calculated scattered ZL flux contributes an uncertainty to the ZL solution of 1.2%. The stability of our ZL solution with airmass indicates that our calculated net extinction, which incorporates the ZL scattering models from the Appendix, has the correct behavior over the night. However there is no way to independently infer the accuracy of the mean net extinction from the *rms* scatter in the ZL solution because the spectral shape of  $\tau_{\text{eff}}(\lambda, t)$  does not change significantly over the night (see Figure A11); an error in the mean level of  $\tau_{\text{eff}}$  will not affect the *rms* scatter in the solution between exposures. The errors in our result are summarized in Table 1. We discuss the systematic uncertainties further in the next section.

## 7. DISCUSSION

The *rms* scatter in our ZL solution is less than 1%. This demonstrates that statistical errors are quite small, be they a result of instrumental effects or our analysis

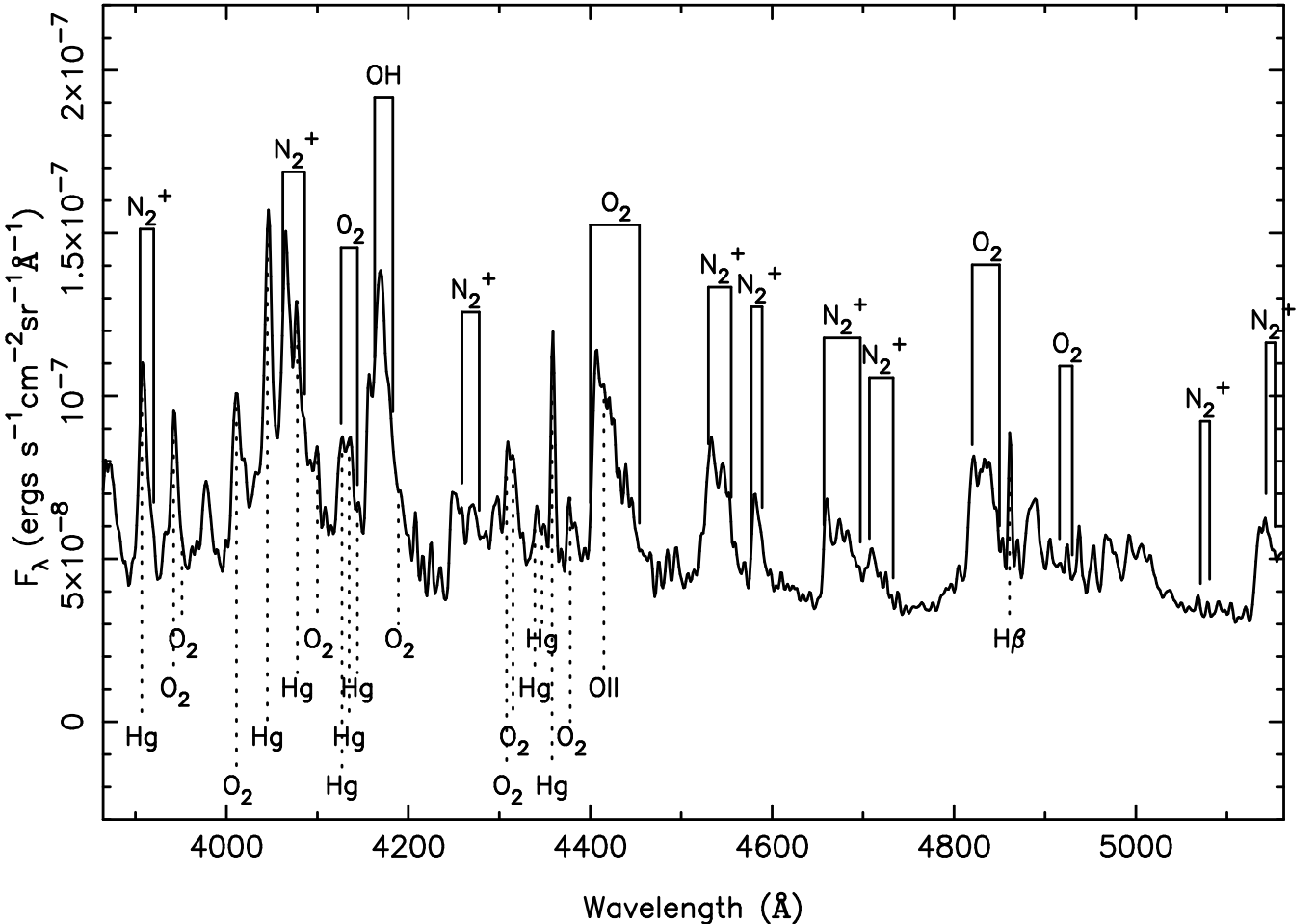


FIG. 14.— Airglow emission lines in the observed spectrum of the night sky after zodiacal light is subtracted. Broad emission features (marked above) are molecular rotation-vibration bands of  $O_2$ ,  $N_2$ ,  $H_2$ ,  $OH$ , and  $NO_2$ . Collisional de-excitation of these molecules contributes a continuum as well. Emission lines (marked below) are also seen in this wavelength range from atomic transitions (photoionized  $O$  and  $Hg$ ).

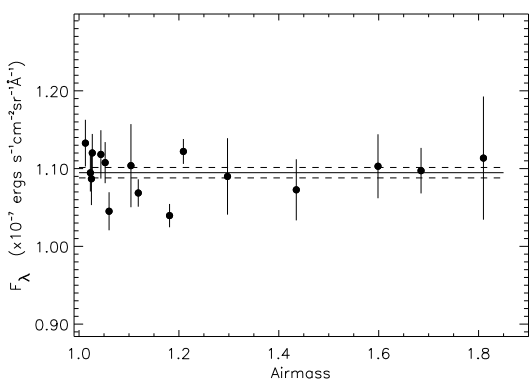


FIG. 13.— The same as Figure 12, but here only the four features with the smallest error bars have been used to produce the mean value of the ZL at 4600–4700 $\text{\AA}$  in each spectrum. The horizontal line shows the mean ZL flux, which is  $109.4(\pm 0.6) \times 10^{-9} \text{ ergs s}^{-1} \text{ cm}^{-2} \text{ sr}^{-1} \text{ \AA}^{-1}$ . Dashed lines show the one-sigma statistical error in the mean (0.6%).

method. Systematic uncertainties due to instrumental ef-

fects are also quite small and are straightforward to quantify (see Table 1). This is demonstrated by the fact that we obtain consistent results to within 0.3% from data taken on two different nights, independently reduced and calibrated. The uncertainties in the atmospheric scattering model described in the Appendix have been considered very carefully and we believe that the adopted uncertainties are conservative. However, the measurement presented here is obviously complex and might be effected by systematic errors which are more difficult to anticipate or quantify.

One such systematic effect might include moonlight or sunlight scattered in the atmosphere. Based on the scattering analysis in the Appendix, it is clear that scattering into the line of sight from any source, even the sun or moon, is negligible when that source is more than 14 degrees below the horizon. All of the observations in this work took place when the sun was more than 18 degrees below the horizon. Although the observations took place several days after new moon, the moon was below the horizon during all of our program observations, and below 14 degrees for all but 1 exposure. In addition, the net effect of such solar-type scattering contributions, if present, would be to *increase* our estimate of the zodiacal light, and con-

sequentially to artificially *decrease* the value of the inferred EBL in Paper I. We do not believe that such scattering is likely to have influenced our results.

As discussed in §§5 and 6, the contamination of solar features by airglow, while introducing a systematic error, would not introduce a *stable* systematic error: the flux of airglow features changes constantly through the night. The stability of our ZL solution in the eight spectral regions we have used demonstrates empirically that airglow is unlikely to have had a significant effect on our results. However, the possibility can't be ruled out and may introduce a systematic error which we cannot quantify and is not included in our estimate of the formal errors.

It is also possible that some Doppler shifting occurs in the ZL spectral features relative to the solar spectrum due to motion of the dust in the zodiacal plane. For that reason, we allowed for a shift in the central wavelength when calculating the correlation but found no measurable offset. We note, also, that the results of this method would not be affected by the slight Doppler broadening which might affect the spectral features of the ZL, because Doppler broadening will not alter the total flux across a feature. The correlation is unaffected by the saw-tooth effect of subtracting features with mismatched widths at the level of the 0.3Å Doppler broadening which is expected at the orientation of these observations (East & Reay 1984). Note also that while the resolution of the input spectra used for calculating the scattered ISL flux is lower than the resolution of our program observations (4Å versus 2.6Å), this will not affect our analysis as long as regions with width  $>>4\text{\AA}$  are used in the analysis. The smallest of our spectral regions is 15Å.

Figure 14 shows the airglow spectrum (the night sky spectrum after zodiacal light is subtracted) we obtain by this method. Emission lines from molecular rotation-vibration bands ( $\text{O}_2$ ,  $\text{N}_2$ ,  $\text{H}_2$ ,  $\text{OH}$ , and  $\text{NO}_2$ ) are labeled, as are some atomic transmission lines ( $\text{O}$  and  $\text{Hg}$ ). Identification of emission features in this range of the spectrum is not complete (see Schmidke *et al.* 1985, Slanger & Huestis 1981, Jones *et al.* 1985 and references therein).

Finally, we note that our measurement of both the mean flux and ZL color are in very good agreement with typical values for the similar viewing geometries quoted in the literature (see the results of Levasseur-Regourd & Dumont 1980, pictured in Figure A4, and Leinert 1998).

## 8. SUMMARY

We have measured the mean surface brightness of the zodiacal light along a single line of sight towards an extragalactic target using ground-based spectrophotometry with a 300 arcsec<sup>2</sup> field of view. The observations were made on 27 and 29 November 1995, simultaneous with HST observations of the same field. The goal of this co-ordinated program is a measurement of the optical extragalactic background light. Because the zodiacal light at optical wavelengths results from sunlight scattered by interplanetary dust concentrated in the ecliptic plane, the flux towards an extragalactic field varies seasonally. Variations in the interplanetary dust cloud with time and the solar cycle may also affect the flux of zodiacal light. The measurement of zodiacal light present here is therefore uniquely relevant to the date and target field.

Our results incorporate explicit calculation of net effect

of atmospheric scattering on terrestrial measurements of the zodiacal light, and show that these effects are small (< 10%) for zodiacal light measurements far from the Sun. We find the mean flux to be  $109.4 \times 10^{-9}$  ergs s<sup>-1</sup> cm<sup>-2</sup> sr<sup>-1</sup> Å<sup>-1</sup> at 4650Å (see Figure 13), and the color to be 5(±1)% redder than the solar spectrum per 1000Å. The statistical uncertainty in the mean flux is 0.6% (1 $\sigma$ ), and the systematic uncertainty is 1.1% (1 $\sigma$ ). We discuss additional systematic effects which might influence this measurement beyond those which are quantified here. Our results are in good agreement with previous measurements of the ZL at similar orientations with respect to the ecliptic plane and scattering geometry (see Leinert *et al.* 1998 for a recent review). This is the only optical measurement to date which isolates the ZL from other uniform backgrounds, including diffuse Galactic light and extragalactic background light. The color of the ZL as a function of the line of sight through the interplanetary dust cloud is further addressed in Paper I.

We thank an anonymous referee for comments which have significantly improved the analysis. We would also like to thank Carnegie Observatories and specifically L. Searle, A. Oemler, and I. Thompson for generous allocations of observing time at Las Campanas Observatory during the course of this work. The observations would not have been successful without the generous efforts of O. Duhalde, E. Cerda, I. Thompson and especially night assistant H. Olivares. We would also like to thank R. Kurucz for kindly providing an electronic version of the solar spectrum and for helpful discussions. We have benefited greatly from discussions with J. Dalcanton, S. Shectman, and A. Williams. J. Dalcanton and I. Thompson provided the data for measurements of the solid angle of the instrument. RAB would like to thank R. Blandford, A. Readhead, and W. Sargent for financial support in the early stages of this work. This work was supported by NASA through grants NAG LTSA 5-3254 and GO-05968.01-94A to WLF and through Hubble Fellowship grant HF-01088.01-97A awarded by STScI to RAB.

## APPENDIX

### ATMOSPHERIC SCATTERING

In this Appendix, we present all scattering calculations and results used in Section 5. Scattering in the atmosphere is a combination of Rayleigh scattering by molecules and Mie scattering by particulates. The scattering due to these two components can be dealt with individually. We begin by describing a general model for the scattering in a spherical atmosphere and then discuss the specific parameters needed to calculate Rayleigh and Mie scattering affecting observations from Las Campanas Observatory. Finally, we present the predicted contribution of scattered light to the program observations analyzed in this paper. We address zodiacal light and the integrated starlight as scattering sources separately.

#### Generic Calculations

The first calculations of radiative transfer in a Rayleigh scattering atmosphere were published by Chandrasekar in 1950. Since then, a number of authors have published ra-

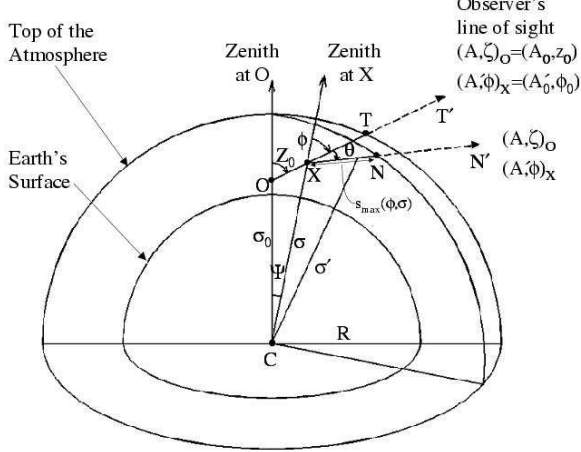


FIG. A1.— Geometry for atmospheric scattering along the line of sight  $OXT$ , with the observer at  $O$  and the line of sight exiting the atmosphere at  $T$ . In the case illustrated, scattering occurs at  $X$  from light entering the atmosphere at  $N$  from  $N'$ .

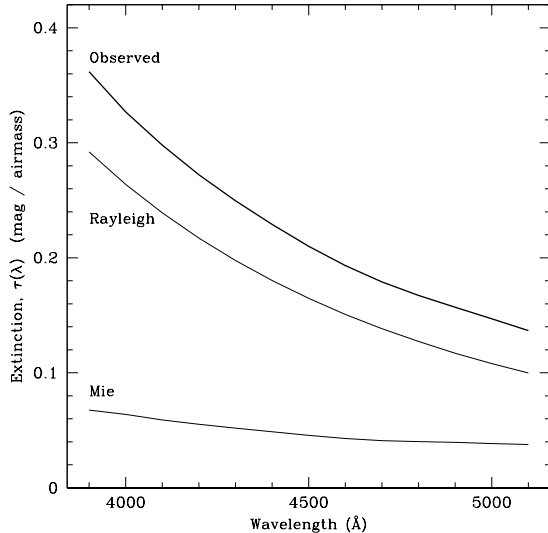


FIG. A2.— We compare the observed extinction,  $\tau(\lambda)$ , derived from observations of standard stars on 1995 November 27 and 29, with the predicted extinction due to Rayleigh scattering, which is well known (see text). The extinction due to Mie scattering is the difference between the two.

diative transfer calculations addressing Rayleigh and Mie scattering in a curved atmosphere (e.g. Sekera 1952, Sekera & Ashburn 1953, and Ashburn 1954), and the effects of multiple-scattering (Dave 1964, de Bary & Bullrich 1964, and de Bary 1964). Careful measurements of zodiacal light over the sky and intensity distributions of the daytime sky have empirically demonstrated the accuracy of those calculations (e.g. Elterman 1966; Green, Deepak, & Lipofsky 1971; Weinberg 1964, Dumont 1965).

To calculate the atmospheric scattering affecting the observations described in this Paper, we begin by adopting the scattering geometry and coordinate system definitions used by Wolstencroft & van Breda (1967, hereafter

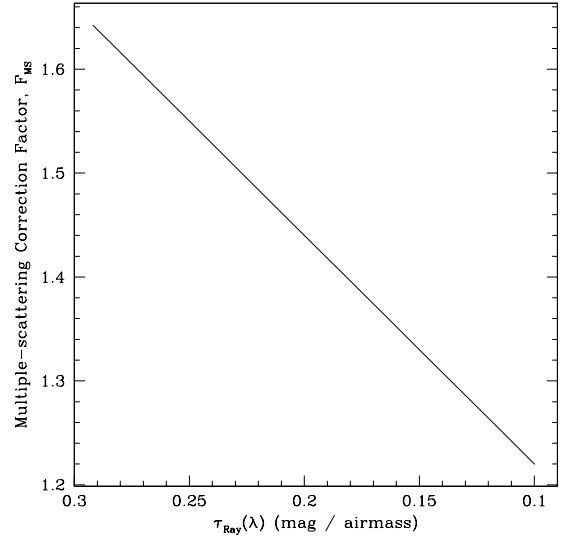


FIG. A3.— Correction factor for multiple scattering,  $F_{\text{MS}}$ , as a function of the Rayleigh extinction.

WvB67), illustrated in Figure A1:  $(A, \zeta)_O$  and  $(A', \phi)_X$  are azimuth/zenith-distance coordinate systems centered on the observer at  $O$  and a generic point,  $X$ , along the line of sight, respectively. The problem is then to calculate the brightness observed at  $O$ , along the line of sight  $(A, \zeta)_O = (A_0, z_0)_O$ .

Following WvB67, scattering occurs at the point  $X$  for radiation which entered the atmosphere at the point  $N$  from the direction  $N'$ , given by  $(A, \zeta)_O$  or  $(A', \phi)_X$ . The light arriving at  $X$  from  $N'$  can be expressed as

$$I_X = L(A', \phi) \sin \phi e^{-C_{\text{ext}}(\lambda)h_1(\phi, \sigma)} ds, \quad (\text{A1})$$

in which the above-the-atmosphere source has flux  $L(A', \phi)$ , light is attenuated by  $e^{-C_{\text{ext}}(\lambda)h_1(\phi, \sigma)}$  as it travels along  $NX$ , and  $s$  is the distance along that path. Attenuation is a function of  $C_{\text{ext}}(\lambda)$ , the extinction cross section of the scattering particles in  $\text{cm}^2$ , and of  $h_1(\phi, \sigma)$ , the effective column density of particles along the line of sight. The effective column density is defined by the local zenith angle,  $\phi$ , and the distance,  $\sigma$ , which defines the point  $X$  relative to the center of the Earth (see Figure A1):

$$h_1(\phi, \sigma) = \int_0^{s_{\text{max}}(\phi, \sigma)} n(\sigma') ds', \quad (\text{A2})$$

in which  $s_{\text{max}}(\phi, \sigma)$  is the distance from  $X$  to the top of the atmosphere at  $N$ , and  $n(\sigma')$  is the atmospheric number density of molecules in  $\text{cm}^{-3}$  as a function of distance from the center of the Earth,  $\sigma'$ , and as a function of the distance  $s'$  along the line  $NX$ .

The light scattered towards the observer from  $X$  is then

$$\frac{3}{16\pi} C_{\text{scat}}(\lambda)n(\sigma)P(\theta) I_X d\phi dA' ds, \quad (\text{A3})$$

in which  $P(\theta)$  is the scattering phase function and  $I_X$ , the flux arriving at point  $X$  is given in Equation A1. Finally, the scattered light is further attenuated by the factor

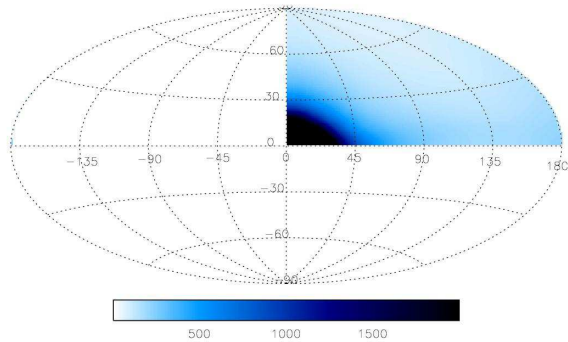


FIG. A4.— Zodiacal light over the sky is plotted in sun-centered ecliptic coordinates, so that the Sun is at  $(\lambda - \lambda_{\odot} = 0^{\circ}, \beta = 0^{\circ})$ , the anti-solar direction is  $(\lambda - \lambda_{\odot} = 180^{\circ}, \beta = 0^{\circ})$ , and the ecliptic poles are at  $\beta = \pm 90^{\circ}$ . All four quadrants are assumed to be the same, which is correct to within a few percent during the time of year when our observations occur.

$e^{-C_{\text{ext}}(\lambda)h_2(z_0, \sigma)}$ , in which

$$h_2(z_0, \sigma) = h_1(z_0, \sigma_0) - h_1(z_0 - \psi, \sigma). \quad (\text{A4})$$

The total flux scattered into the line of sight  $(z_0, A_0)$  from sources distributed over entire visible hemisphere of the sky is then

$$I_{\text{scat}}(z_0, A_0) = \frac{3C_{\text{scat}}(\lambda)}{16\pi} \int_{s=0}^{s_{\text{max}}(z_0, \sigma_0)} \int_{\phi=0}^{\pi/2+f(\sigma)} \int_{A'=0}^{2\pi} n(\sigma) P(\theta) L(A', \phi) \sin \phi e^{-C_{\text{scat}}(\lambda) [h_1(\phi, \sigma) + h_2(z_0, \sigma)]} d\phi dA' ds. \quad (\text{A5})$$

The visible sky at the point  $X$  dips below the observer's horizon at large values of  $s$ . Hence, the limit of the integral over  $\phi$ , is greater than  $\phi/2$  by the value  $f(\sigma) = \cos^{-1}(R/\sigma) \leq 14^{\circ}$ , where  $R$  is the radius of the Earth (6371 km). The equations needed to change variables between  $(A', \phi)$  and  $(z_0, A_0)$  are given WvB67.

The phase function for Rayleigh scattering is  $P(\theta) = 1 + \cos^2(\theta)$ . The atmospheric density is given by the standard barometric formula  $n(\sigma) = n_0 e^{-H/H_0}$ , where  $H$  is the altitude above sea level ( $H = \sigma - R$ ), the scale height is  $H_0 = 7.99$  km, the density at sea level is  $n_0 = 2.67 \times 10^{19} \text{ cm}^{-3}$ , and the effective scattering cross-section for air is  $C_{\text{scat}} = 7.78 \times 10^{-27} (\lambda/4600 \text{ \AA})^{-4} \text{ cm}^2$  (see Schubert & Walterscheid 1999 and van de Hulst 1952). For molecules in the atmosphere, extinction is entirely due to scattering, so that  $C_{\text{ext}} = C_{\text{scat}}$ . Atmospheric extinction due to Rayleigh scattering is then  $\tau^R(\lambda) = C_{\text{ext}}(\lambda) \int_R^{\infty} n(\sigma) d\sigma$ . For the duPont telescope at Las Campanas, which is at an altitude of 2.28 km, the expected Rayleigh extinction is  $\tau^R(4600 \text{ \AA}) = 0.12$ .

The phase function for Mie scattering by particulates in the atmosphere depends on the distribution of particle sizes, and must be empirically determined. We adopt the phase function measured by Green, Deepak & Lipofsky (1971) from their complete analysis of the Mie (particulate) scattering and Rayleigh (molecular) scattering components of the atmosphere based on the scattering of

sunlight. Their results are in good agreement with theoretical scattering models and other estimates of the size-distribution of particles in the atmosphere and have a negligible dependence on wavelength for our purposes (see Elterman 1966, and Deepak & Green 1970). The scattering and extinction coefficients for particulate scattering are a function of the size distribution of particles and vary with time and geography. The extinction due to Mie scattering can, however, be inferred from the observed extinction for a point source and the calculated Rayleigh extinction coefficient:  $\tau^M = \tau_{\text{obs}} - \tau^R \sim 0.05$  at 4500 \AA (see Figure A2). This value is in good agreement with estimates for Tenerife by Dumont (1965) and for Haleakala by Weinberg (1964). This is not surprising as our observed  $\tau_{\text{obs}}(\lambda)$  is consistent with the CTIO curves (Baldwin & Stone 1984, Stone & Baldwin 1983), and  $\tau^R(\lambda)$  is simply a function of the atmospheric density.

Unlike the case for molecules, the attenuation caused by particulates is not entirely due to scattering. Staude (1975) adopts values of  $C_{\text{scat}} = 4.47 \times 10^{-11} \text{ cm}^2$  and  $C_{\text{ext}} = 7.53 \times 10^{-11} \text{ cm}^2$  for dry air at 4200 \AA. With a sea level density of  $n_0 = 1.11 \times 10^4 \text{ cm}^{-3}$ , and a distribution scale height of only  $h_0 = 1.2$  km, these parameters give  $\tau^M \sim 0.01$  at 2 km. We have scaled  $C_{\text{scat}}$  and  $C_{\text{ext}}$  to give values consistent with our observed value of  $\tau^M$ . Scaling  $H_0$  or assuming a different value of  $H$  would have the same effect on  $I_{\text{scat}}^M(\lambda, \text{ZL})$ .

The scattering model discussed above describes a single scattering event. However, multiple scattering events become significant for scattering angles  $\theta \gtrsim 30^{\circ}$  (de Bary 1964, de Bary & Bullrich 1964). Consequently, we apply a multiple scattering correction for Rayleigh scattering which is adopted from Dave (1964) and plotted in Figure A3. The correction factor plotted in Figure A3 is simply the factor by which the intensity of scattered light increases over the single-scattering case. Multiple scattering does not occur due to particulates (Mie case) because of the small scattering angles which dominate that process and very small values of  $\tau^M(\lambda)$ .

To confirm the accuracy of our calculations, we checked our scattering model against published results of Staude (1975), WvB67, and Ashburn (1954) for a uniform, sky-filling source of unit flux. We find that our results are consistent to within 4% for zenith angles  $z \leq 80^{\circ}$  before the multiple scattering correction is applied. (WvB67 predates evidence for the effects of multiple scattering, and Staude adopts the same corrections used here.) The uncertainty in the multiple scattering correction is roughly 4–7%, increasing with larger values of  $\tau$ .

Using the expressions above, we calculate the scattered light flux,  $I_{\text{scat}}(\lambda)$ , resulting from Mie scattering by particulates and Rayleigh scattering by molecules throughout the nights of our observations. The results depend explicitly on the absolute position of the Sun and the Galactic center relative to the observatory and relative to the target field. In the following sections, we consider the cases of zodiacal light (ZL) and integrated starlight (ISL) as the extra-terrestrial source of flux separately.

### Zodiacal Light

To calculate the scattered zodiacal light along the line of sight of our observations, we adopt values for the zodiacal flux given in Leinert *et al.* (1998), which are taken

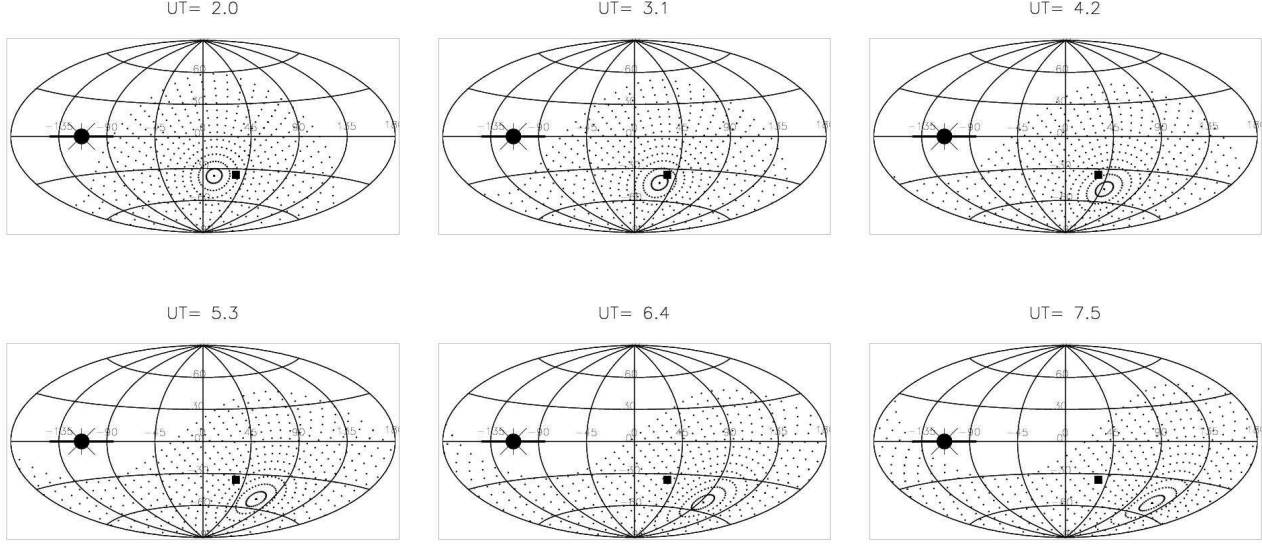


FIG. A5.— Integration pattern for calculating scattered zodiacal light. Each plot is an Aitoff projection of the sky in Ecliptic coordinates. The position of the Sun and the ecliptic plane are indicated by the Sun symbol with a bar through it. Obviously, the ecliptic plane is along the  $0^\circ$  latitude line. Our target field is indicated by the square. The ecliptic coordinates of the zenith can be seen as the “bullseye” center of the integration pattern. The motion of the target relative to the local zenith is clear as the target moves from east to west of the zenith point in the integration pattern. The coordinates of the local horizon are traced by the edge of the integration pattern. The Sun is obviously located just to the west of the horizon at the start of the night (UT=2.0 hr) and just to the east of the horizon at the end of the observing night (UT=7.5 hr).

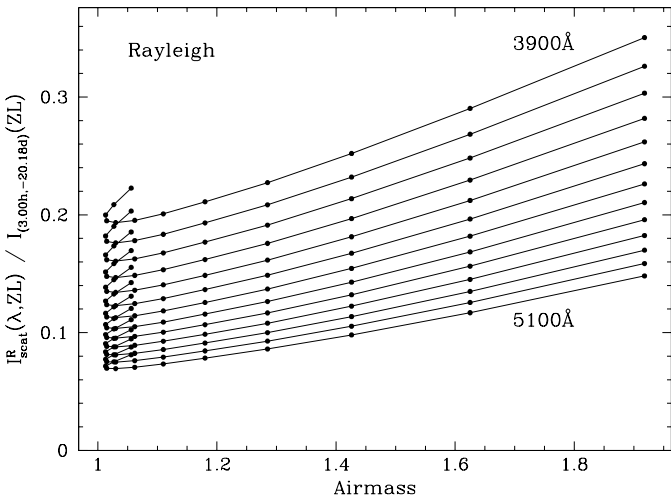


FIG. A6.— The Rayleigh scattered zodiacal light contribution to our observed night sky flux on the nights of 1995 November 27-29 as a function of airmass at 100Å intervals from 3900Å to 5100Å. Flux decreases monotonically with wavelength at any airmass, following the behavior of  $\tau^R(\lambda)$ .  $I_{\text{scat}}^R(\lambda, \text{ZL})$  is given as a fraction of the above-the-atmosphere zodiacal light flux in our target field; this removes the spectrum of the zodiacal light itself and emphasizes the wavelength dependence of the scattering. The each line shows the change in  $I_{\text{scat}}^R(\lambda, \text{ZL})$  as the target field goes from slightly east of zenith, through zenith, to far west of zenith during the night. Dots mark half-hour intervals between UT=2.0 hr and UT=7.5 hr.

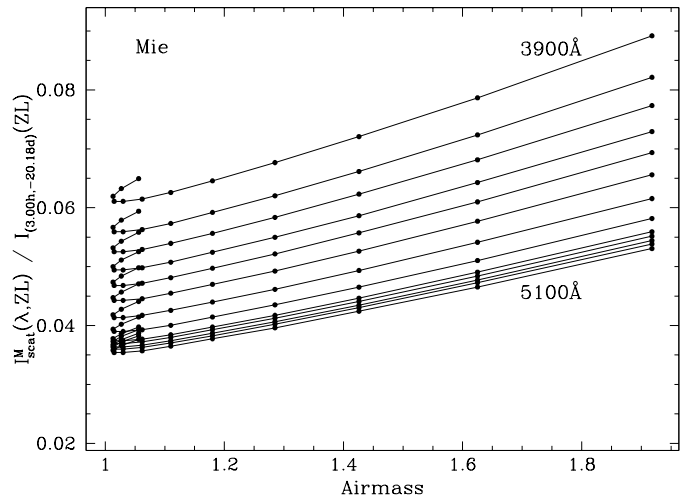


FIG. A7.— Same as Figure A6, but here we plot the contribution of Mie scattered zodiacal light along the line of sight. Again, the scattered light flux is plotted as a fraction of the above-the-atmosphere zodiacal light flux in our target field.

from Levasseur-Regourd & Dumont (1980) with values at elongations  $\epsilon < 30^\circ$  added from space-based observations. These ZL values are above-the-atmosphere fluxes and are in excellent agreement with later space-based results (see Leinert *et al.* 1981). To obtain a smooth flux distribution of ZL on the sky (see Figure A4), we use the spherical

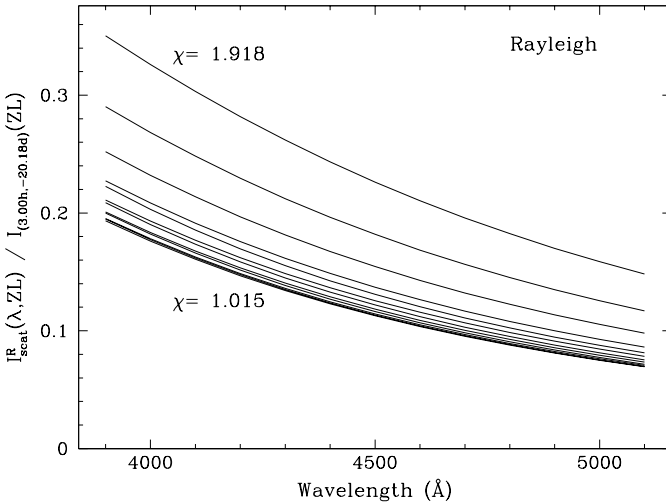


FIG. A8.— Same as Figure A6, but here each line indicates  $I_{\text{scat}}^R(\lambda, \text{ZL})$  as a function of wavelength at discrete times. Scattering is maximized at high airmass (far west of zenith), and minimized slightly west of zenith, when the airmass is still relatively low and the Sun has had time to set far enough that highest flux regions of zodiacal light are no longer in the visible hemisphere of the sky.

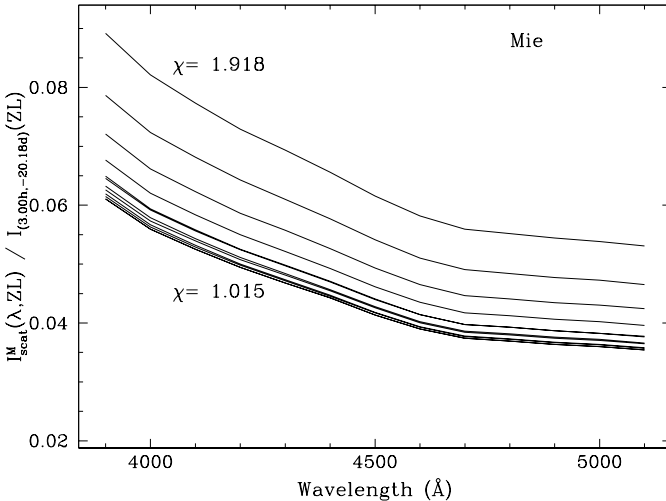


FIG. A9.— Same as Figure A8, but showing the Mie scattered zodiacal light.

interpolation method developed by Renka (1997).

In Figure A5, we show the integration pattern in  $\phi$  (zenith angle) and  $A'$  (azimuth) used to calculate  $I_{\text{scat}}(\lambda, \text{ZL})$  (Equation A6) at the indicated times during the nights of our observations. Actual calculations were done with twice the number of integration points shown in the figures. The visible part of the sky (shown by the integration pattern) is at least 30 degrees from the Sun during our observations.

As a technical detail, we have made the simplifying assumption that the spectral shape of the ZL over the visible hemisphere is uniform. That is, only the mean flux of the ZL changes. Although there are variations in the color (de-

fined in Equation 1) of the ZL over the range 3900-5100\text{\AA} from  $\epsilon = 30^\circ$  to  $\epsilon = 180^\circ$ , the total change is empirically less than  $\sim 8\%$  and our target is in the center of the expected color range (e.g., Frey *et al.* 1974, Leinert *et al.* 1981). We have run trail scattering models in which we change the flux with  $\epsilon$  over the sky by  $\pm 4\%$ , and we find that the effect on the predicted scattered flux is changed by 0.4% at airmasses higher than 1.6, and 0.2% at the lowest airmass. In other words, by ignoring the color variation in ZL over the sky, the scattered light model will be wrong by 0.2% at 3900\text{\AA} relative to the value at 5100\text{\AA}, or  $\pm 0.1\%$  over the range 3900-5100\text{\AA} for our observing situation (positions of the Sun relative to the target and the horizon).

The predicted Rayleigh and Mie scattering flux of ZL,  $I_{\text{scat}}^R$  and  $I_{\text{scat}}^M$ , respectively, along the line of sight to our target field throughout our observations is shown in Figures A6-A9. In those Figures, we show the scattered light as a function of the above-the-atmosphere ZL flux in target field at ( $\alpha = 3.00h, \delta = -20.18d$ ),  $I_{(3h, -20d)}(\text{ZL})$ . This removes the spectrum of the ZL and highlights the wavelength dependence of  $I_{\text{scat}}$ . The predicted scattered flux is not symmetric about the zenith because the distribution of ZL over the sky is not symmetric: the scattered light will be smaller at the same airmass if the Sun is further below the horizon, i.e. the middle of the night. The scattered flux is therefore minimized near UT $\sim 4$ , when the field is still at low airmass and the brightest regions of the ZL are below the horizon. In Figure A10, we show the total combined effect of the atmosphere on the ZL flux received from the target field:

$$I_{\text{net}}(\lambda, t, \chi, \text{ZL}) = I_{\text{scat}}^R(\lambda, t, \chi, \text{ZL}) + I_{\text{scat}}^M(\lambda, t, \chi, \text{ZL}) - I_{(3h, -20d)}(\lambda, \text{ZL})(1 - e^{-\tau_{\text{obs}}(\lambda)\chi}). \quad (\text{A6})$$

Finally, from  $I_{\text{net}}(\lambda, \text{ZL})$  we can calculate an *effective* extinction for the ZL from our target field at the specific times at which our observations occurred. The effective extinction is defined by the equation

$$I_{\text{net}}(\lambda, t, \chi, \text{ZL}) = (1 - e^{\tau_{\text{eff}}(\lambda, t)\chi})I_{(3h, -20d)}(\lambda, \text{ZL}) \quad (\text{A7})$$

The effective extinction is plotted in Figure A11, and is specific to our target field, times of observation, observed extinction, geographic latitude and longitude, and altitude.

The result which is applied to our ZL measurement from the modeling discussed here is  $\tau_{\text{eff}}(\lambda, t)$ , which corresponds to  $I_{\text{net}}(\lambda, t, \chi, \text{ZL})$  rather than  $I_{\text{scat}}(\lambda, t, \chi, \text{ZL})$ . The virtue of this approach is that the absolute flux accuracy of the adopted ZL over the sky (Fig. A4) does not affect our results; only the accuracy of the *relative* flux distribution over the sky matters. In the regions of the sky which dominate the scattering for our observations (solar elongations of  $\epsilon > 30^\circ$ ), the relative flux errors for the ZL over the visible hemisphere of the sky are  $\leq 5\%$  over large areas ( $> 30^\circ$ ), and better on small scales. Such errors will propagate into final measurement of the ZL at the level of  $< 1\%$  at high airmass, and  $< 0.4\%$  at low airmass. Nevertheless, we note that the above-the-atmosphere value of the ZL from Levasseur-Regourd & Dumont (1980) agrees with our measurement in our target field to within 2%.

To evaluate the accuracy of our calculated values of  $I_{\text{net}}(\text{ZL})$  (see Equation A7), we estimate that the uncer-

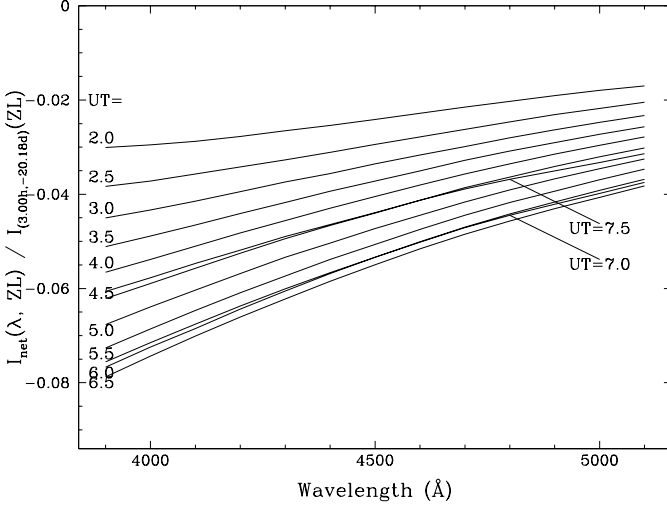


FIG. A10.— The net effect of the atmosphere on the observed spectrum of zodiacal light.  $I_{\text{net}}(\text{ZL})$  is the flux received from the target field plus the scattered light coming from the entire visible hemisphere of the sky:  $I_{\text{net}}(\lambda, \text{ZL}) = I_{\text{scat}}(\lambda, \text{ZL}) - I_{(3h,-20d)}(\text{ZL}) (1 - e^{-\chi\tau(\lambda, \text{obs})})$ .  $I_{\text{net}}(\lambda, \text{ZL})$  is plotted as a function of wavelength at discrete times, as labeled. Flux units are the same as in Figures A6 – A9.

tainty in our scattering calculations is 8% at the low zenith angles ( $< 30^\circ$ ) where the bulk of our observations occur. This estimate is based on the comparisons between scattering models and atmospheric measurements presented in Green *et al.* (1971), Dave (1964), and Staude (1975), and is consistent with the uncertainties discussed in WvB67, Ashburn (1954), and Sekera & Ashburn (1953). The time-weighted average of  $I_{\text{scat}}(\text{ZL})$  over the course of our observations is  $\sim 0.15 \times I_{(3h,-20d)}(\lambda, \text{ZL})$ , so  $I_{\text{scat}}(\text{ZL})$  has an uncertainty of 1.2% of the ZL flux in our target field. The uncertainty in the observed extinction is much less than 1% and adds negligibly to this error. See §6 for further discussion of the accuracies of the zodiacal light measurement.

We can also assess the accuracy of  $\tau_{\text{eff}}(\lambda)$  independently from our own data, as discussed in §5. Notice that  $I_{\text{net}}(\text{ZL})$  changes with time in a way which is only weakly dependent on wavelength. A consistent solution for the ZL with both wavelength and airmass will be strong confirmation of the accuracy of the values for  $\tau_{\text{eff}}(\lambda, t)$  calculated here.

#### Integrated Starlight

Unlike the scattered ZL, the scattering which results from integrated starlight (ISL) must be incorporated into our analysis of the observed night sky spectrum as an absolute flux value. We must therefore first derive a spectrum for the ISL as a function of position over the sky. To do so, we have followed the method suggested by Mattila (1980a, 1980b), which we briefly summarize here.

The spatial and flux distribution of stars of all spectral types can be described by exponential distributions perpendicular to the Galactic plane (in the  $z$  direction) and narrow Gaussian distributions in intrinsic magnitude. The mean emission per  $\text{pc}^3$  from stars of type  $i$  as a function

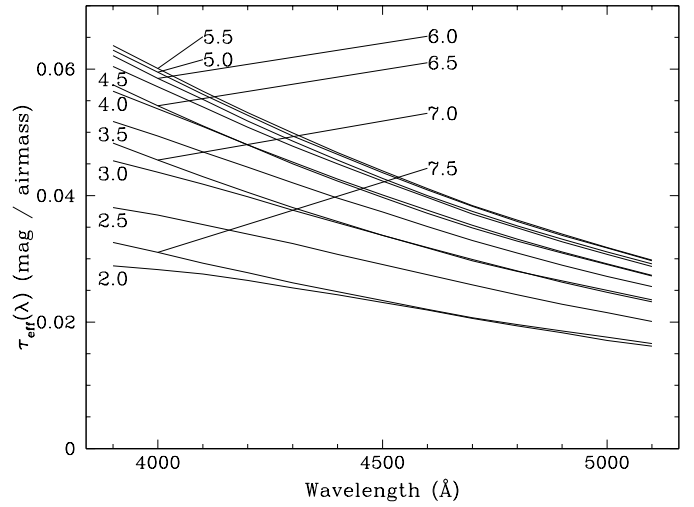


FIG. A11.— Each line shows the effective extinction for the zodiacal light as a function of wavelength for our observations at the indicated UT. The effective extinction corresponds to the net loss of light relative to the above-the-atmosphere flux of the zodiacal light in our field of view (see Figure A10). For comparison with the total observed extinction derived from standard stars see Figure 4.

of distance from the Galactic plane,  $z$ , can be written as

$$j_i(z) = j_i(0)e^{-|z|/h_i} = D_i(0)10^{-0.4M_i}e^{-|z|/h_i}, \quad (\text{A8})$$

in which  $D_i(0)$  is the number density of stars per cubic parsec in the plane,  $h_i$  is the scale height of the vertical distribution, and  $M_i$  is the mean absolute magnitude of the spectral type  $i$ . The observed flux is also attenuated by interstellar extinction, which can be expressed by a two-component extinction law characterized by a total extinction  $a_0(\lambda) = a_1(\lambda) + a_2(\lambda)$ , with  $a_1(\lambda) : a_2(\lambda)$  in the ratio 1.84 : 0.62 (Neckel 1965). The  $z$ -dependence of extinction can be written as

$$a(z, \lambda) = a_1(\lambda)/[1 + (z/20)^2] + a_2(\lambda)/[1 + (z/100)^2] \quad (\text{A9})$$

for  $z$  given in parsecs (Neckel 1965, Neckel 1980). We find a good fit to the observed ISL by adopting standard values for  $a_0(\lambda)$  (Zombeck 1990), scaled to  $a_0(V) = 1.5 \text{ mag kpc}^{-1}$ .

In cylindrical coordinates, the flux per unit solid angle ( $\text{ergs s}^{-1} \text{cm}^{-2} \text{sr}^{-1} \text{\AA}^{-1}$ ) from stars fainter than  $m_0$  along the line of sight at Galactic latitude  $b$  can be expressed by the volume integral

$$I_\lambda(b) = \sum \frac{j_i(0)f_i(\lambda)}{4\pi \sin b} \int_{z_0}^{\infty} e^{-z/h_i} 10^{-0.4A_\lambda(z)/\sin b} dz, \quad (\text{A10})$$

in which  $r$  is the distance along the line of sight from the observer in parsecs and  $f_i$  is the spectral energy density of a star of type  $i$  in  $\text{ergs s}^{-1} \text{cm}^{-2} \text{\AA}^{-1}$ . In the derivation of the above integral, the  $1/4\pi r^2$  loss of flux from each star along the line of sight has canceled with the  $r^2 d\Omega$  in the volume integral, and we have changed variables using the relation  $r = z/\sin b$ . The lower limit of integration is simply the distance modulus for stars of each type corresponding to the bright magnitude cut-off,  $m_0$ , so that

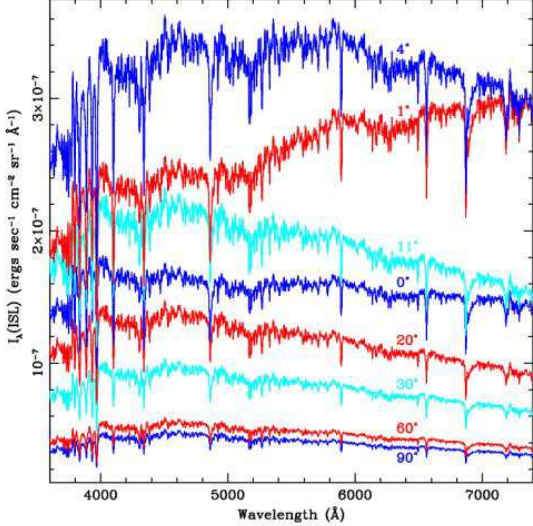


FIG. A12.— The mean integrated starlight (ISL) spectra as a function of Galactic latitude (as labeled) produced by the model described §A.3.

$z_0 = 10^{0.2(m_0 - M_i + 5)}$  in parsecs. Finally, the extinction from  $z$  to the observer is

$$\begin{aligned} A_\lambda(z) &= \int_0^z a(z) dz \\ &= 20a_1(\lambda) \arctan(z/20) + 100a_2(\lambda) \arctan(z/100). \end{aligned} \quad (\text{A11})$$

Using 33 individual stellar types described by the parameters  $M_i$ ,  $D_i$ , and  $h_i$  from Wainscoat *et al.* (1992), we obtain integrated spectra which agree with the observed star counts at  $V$  and  $B$  (Roach & Megill 1961, see also Allen 1973) to  $m_0 = 6$  V mag at  $|b| > 5^\circ$  to better than 10%, which is more than adequate for our purposes. The spectral energy densities for each stellar type,  $f_i(\lambda)$  were obtained from the STScI archive (Jacoby, Hunter, & Christian 1984) and have a resolution of roughly 4Å. We include stars by type with  $m_0 < 6$  V mag from the SAO star catalog by hand. We felt this was necessary as the statistical variation in stellar density on small scales around the solar neighborhood can have a significant impact on the accuracy of the model, while variations are apparently averaged out in stellar populations at large distances. In Figure A12, we plot the total integrated starlight (ISL) with no bright magnitude cut off at  $0^\circ < |b| < 90^\circ$ . The total flux at  $|b| = 90^\circ$  is roughly  $20 \times 10^{-9}$  ergs  $s^{-1} cm^{-2} sr^{-1} \text{Å}^{-1}$ , while the flux near the plane is as high as  $300 \times 10^{-9}$  ergs  $s^{-1} cm^{-2} sr^{-1} \text{Å}^{-1}$ . Interstellar extinction limits the ISL flux in the plane in our model, probably more than is appropriate. However the flux rises rapidly even  $1^\circ$  degree above the plane to more realistic values. The limited sky area at  $b = 0^\circ$  precludes this from impacting the accuracy of the models.

Figure A15 shows the total scattered ISL flux due to Rayleigh and Mie scattering which contributes to observations of our target field at the beginning of the observing night (UT=2.0 hr). The total flux ( $\sim 12 \times 10^{-9}$  ergs  $s^{-1} cm^{-2} sr^{-1} \text{Å}^{-1}$ ) is roughly 12% of the ZL flux above the

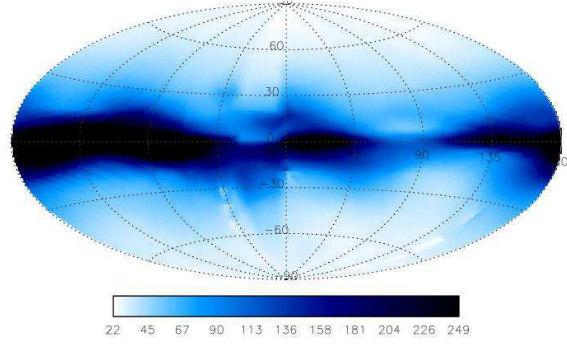


FIG. A13.— Integrated starlight over the sky from star counts at  $V$ . Flux units are  $1 \times 10^{-9}$  ergs  $s^{-1} cm^{-2} sr^{-1} \text{Å}^{-1}$ .

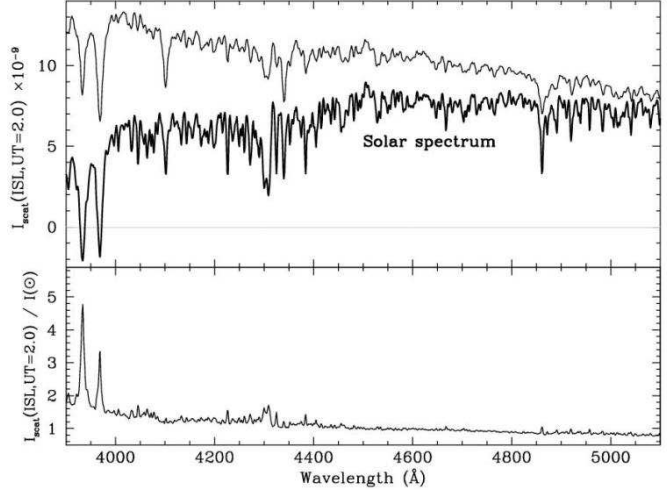


FIG. A15.— The upper plot shows the predicted spectrum of the scattered ISL along the line of sight to the EBL field at UT=2.0 hr for our observations. Units are  $\text{ergs s}^{-1} \text{cm}^{-2} \text{sr}^{-1} \text{Å}^{-1}$ . The solar spectrum is also shown, scaled to the same flux and offset, to allow visual comparison of the spectral features. The lower plot shows the ratio of that spectrum to the solar spectrum, normalized at 4600Å, the center of our observed wavelength range. Note that the total flux from the scattered ISL in this case is < 5% of the total flux of the combined zodiacal light and airglow, and the spectral features are weaker in the scattered ISL.

atmosphere in our target field. The ISL flux in the observed sky spectrum will impact our measurement of the ZL flux only if the ISL spectrum has the same features as the solar (zodiacal light) spectrum. In the lower plot of Figure A15, we therefore plot ratio of the  $I_{\text{scat}}(\lambda, t, \chi, \text{ISL})$  to the solar spectrum, normalized at 4600Å. It is clear from this plot that the scattered ISL and solar spectra differ by 5–10% at  $> 4500\text{Å}$ , but by a factor of 3–5 in the strength of spectral features at less than 4500Å. In Figure A16, we plot the ratio of  $I_{\text{scat}}(\lambda, t, \chi, \text{ISL})$  throughout the night to  $I_{\text{scat}}(\lambda, t, \chi, \text{ISL})$  at UT=2.0 hr. From this plot it is clear that strength of spectral features changes only very weakly throughout the night, by < 1% over the majority of the spectrum and by < 4% at 3900–4000Å (CaI H &

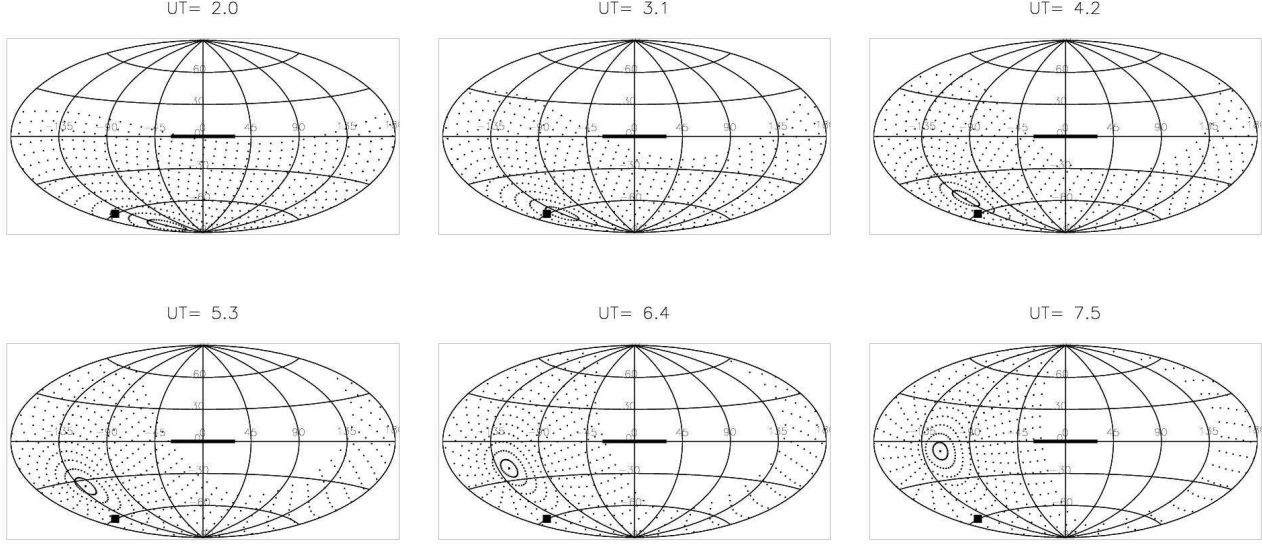


FIG. A14.— Integration pattern for the calculation of scattered ISL flux. Each plot is an Aitoff projection of the sky in Galactic coordinates. The center of the Galaxy is at the center of each plot ( $l = 0^\circ, b = 0^\circ$ ). The Galactic plane within 30 degrees of the Galactic center is marked by the thick line. Our target field is indicated by the square. The Galactic coordinates of the zenith can be seen as the “bullseye” center of the integration pattern. The coordinates of the local horizon are shown by the edge of the integration pattern. The Galactic plane is running along the horizon at the start of the night (UT=2.0 hr), and is perpendicular to the horizon at the end of the night (UT=7.5 hr). The Galactic center is never above the horizon. See Figure A5 for further discussion.

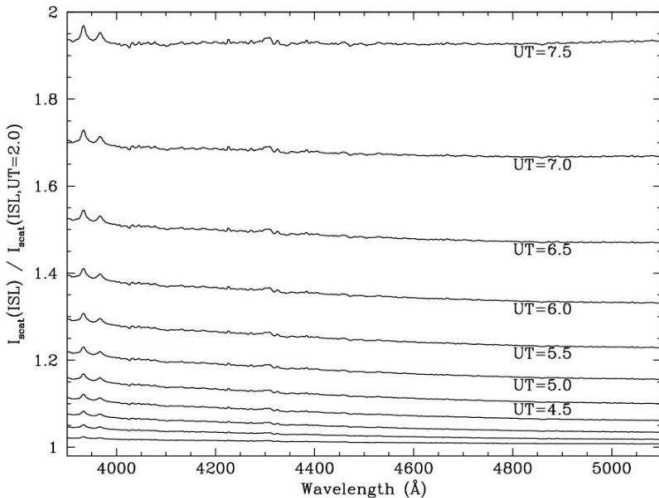


FIG. A16.— The ratio of the predicted scattered ISL spectrum at the indicated UT on the night of our observations, relative to the predicted spectrum at UT=2.0 hr. The plot demonstrates that relatively small changes (< 4%) occur in the strength of individual spectral features over the night, while changes in broad-band color and mean flux are significant.

K). The consistency of our ZL measurement (§6) over the full wavelength range 3900–5100Å is, therefore, a strong test of the accuracy of the predicted contribution of scattered ISL. As discussed in §5, the predicted scattered ISL flux is entirely consistent with our observations. See §5 for further discussion.

Obviously, the model we describe above makes no allowance for variation in the ISL with Galactic longitude. For comparison, we show in Figure A13 an Aitoff projection of the ISL from star counts over the sky, which shows that the ISL has only minor dependence on longitude at  $b > 20^\circ$ . At lower latitudes where the variation is greater with longitude, the spectroscopic model we employ does give a good approximation to the average ISL. Because the contribution to the scattering comes from a wide spread in longitude (compare Figures A14 and A13), the mean value is adequate for our purposes. To test this, we ran simulations in which we maintained the mean ISL flux with latitude, but varied the ISL flux with longitude by  $\pm 25\%$ . We find that the total scattered ISL is affected by less than 9% throughout the night due to longitudinal variations around the mean.

The mean flux in our models for the ISL is consistent with the star counts of Roach & Megill (1961) to within  $\pm 10\%$  at both  $V$  and  $B$ . As in the previous section, we estimate that the uncertainty in our scattering calculations is 8% at the low zenith angles ( $< 30^\circ$ ) where the bulk of our observations occur. Combining these, we estimate the uncertainty in  $I_{\text{scat}}(\lambda, t, \chi, \text{ISL})$  to be 13%. As the relative mean strength of spectral features in starlight is 0.6–4% of the total ZL flux in our target field at the 4000–5200Å, this corresponds to an uncertainty of < 0.5%.

Any significant errors in our model, either in mean flux as might be caused by longitudinal variations in the ISL, or in the spectral energy distribution, would show up as inconsistencies in the solution for the ZL flux as a function of wavelength. Furthermore, errors would be worst at higher airmass, where Figure A14 shows that the low-galactic-latitude sky has a greater impact on the scattered ISL,

the mean flux is greater, and the stellar-type mix is more sensitive. No such variations with wavelength are found, as we have discussed in §5. See §6 for further discussion of the accuracies of the zodiacal light measurement.

## REFERENCES

Allen, C.W. 1973, *Astrophysical Quantities*, (London: Athlone Press), 244

Ashburn, E.V. 1954, *J. Atm. Terrest. Phys.*, 5, 83

Baldwin, J.H. & Stone, R.P.S. 1984, *MN*, 206, 241

Beggs, D.W., Blackwell, D.E., Dewhirst, D.W., & Wolstencroft, R.D. 1964, *MN*, 127, 329

Bernstein, R.A., Freedman, W.L., Madore, B.F. 2002a, *ApJ*, in press (Paper I)

Bernstein, R.A., Freedman, W.L., Madore, B.F. 2002c, *ApJ*, in press (Paper III)

Berriman, G.B., Boggess, N.W., Hauser, M.G., Kelsall, T., Lisse, C.M., Moseley, S.H., Reach, W.T., & Silverberg, R.F. 1994, *ApJ*, L63

Brownlee, D.E. 1978, in *Cosmic Dust*, ed. A.M. McDonnell (New York: Wiley and Sons), 295

Chandrasekhar, S. 1950, *Radiative Transfer*, (Oxford: Oxford Univ. Press).

Dave, J.V. 1964, *J. Opt. Soc. America*, 54, 307

de Bary, E. & Bullrich K. 1964, *J. Opt. Soc. America*, 54, 1413

de Bary, E. 1964 *Appl. Opt.*, 3, 1293

Deepak, A., Green, A.E.S. 1970, *Appl. Opt.*, 9, 2362

Dermott, S.F., Jayaraman, S., Xu, Y.L., Grogan, K. & Gustafson, B.A.S. 1996, in *AIP Conference Proceedings No. 348, Unveiling the Cosmic Infrared Background*, ed. E. Dwek (Woodbury, NY: AIP Press), 25

Dube, R.R., Wickes, W.C. & Wilkinson, D.T. 1979, *ApJ*, 232, 333

Dumont, R. 1965, *Ann. Astrophys.*, 28, 265

East, I.R. & Reay, N.K. 1984, *AA*, 139, 512

Elterman, L. 1966, *Appl. Opt.*, 5, 1769

Fechtig, H., Hartung, J.B., Nagel, K., Neukum, G., & Storzer, D. 1974, in *Proc. Fifth Lunar Sci. Conf., Geochem. Cosmochem. Sup.*, 5, 3, 2463

Filippenko, A.V. 1982, *PASP*, 94, 244

Frey, A., Hofmann, W., Lemke, D. & Thum, C. 1974, *A&A*, 36, 447

Gilliland, R.L. 1992, in *ASP Conference Series Vol. 23, Astronomical CCD Observing and Reduction Techniques*, ed. S.B. Howell (San Francisco: BookCrafters, Inc.), 68

Girard, T.M., Grundy, W.M., Lopez, C.E., & Van Altena, W.F. 1989, *AJ*, 98, 227

Green, A.E.S., Deepak, A., Lipofsky, B.J. 1971, *Appl. Opt.*, 10, 1263

Hamuy, M., Walker, A.R., Suntzeff, N.B., Gigoux, P., Heathcote, S.R. & Phillips, M.M. 1992, *PASP*, 104, 553

Hayes, D.S. & Laytham, D.W. 1975, *ApJ*, 197, 587

Hayes, D.S. 1985, in *IAU Symposium No. 111, Calibration of Fundamental Quantities*, eds. D.S. Hayes, L.E. Pasinetti, & A.G. Davis Phillip (Reidel, Dordrecht), 225

Jacoby, G.H., Hunter, D.A., Christian, C.A. 1984, *ApJS*, 56, 257

Johnson, H.L. & Harris III, D.L. 1954, *ApJ*, 120, 196

Jones, A.V., Meier, R.R., Shefov, N.N. 1985, *J. Atmosph. Terrest. Phys.*, 47, 623

Kurucz, R.L., Furenlid, I., Brault, J., & Testerman, L. 1984, *Solar Flux Atlas from 296 to 1300 nm, National Solar Observatory Atlas No. 1 (Sunspot: National Solar Observatory)*

Leinert, Ch., Richter, I., Pitz, E., Planck, B. 1981, *A&A*, 103, 177

Leinert, Ch., *et al.* 1998, *AAS*, 127, 1

Levasseur-Regourd, A.C. & Dumont, R. 1980, *AA*, 84, 277

Matsuura, S., Matsumoto, T., & Matsuhara, H. 1995, *Icarus* 115, 199

Mattila, K. 1980, *AA&S*, 39, 53 (1980a)

Mattila, K. 1980, *A&A*, 82, 373 (1980b)

Martin, C., Hurwitz, M. & Bowyer, S. 1991, *ApJ*, 379, 549

Neckel, Th. 1965, *ZA*, 63, 221

Neckel, Th., Klare, G., Sarcander, M. 1980, *A&AS*, 42, 251

Neckel, H. & Labs, D. 1984, *Sol. Phys.*, 90, 205

Press, W., Teukolsky, S., Vetterling, W., & Flannery, B. 1992, *Numerical Recipes*, (2d ed.; Cambridge: Cambridge Univ. Press)

Reach, W.T., Abergel, A., Boulanger, F., Désert, Perault, M., Bernard, J.P., Bloommaert, J., Desarsky, C., Cesarsky, D., Metcalfe, L., Puget, J.L., Sibille, F., Vigroux, L. 1996, *AA*, 315, L381

Renka, R.J. 1997, *ACM Transactions on Mathematical Software*, 23, 435

Reynolds, R.J. 1990, in *IAU Symposium No. 139, Galactic and Extragalactic Background Radiation*, ed. S. Bowyer & Ch. Leinert (Dordrecht: Kluwer), 159

Richter, I., Leinert, Ch., & Planck, B. 1982, *AA*, 110, 115

Roach, F.E. & Meinel, A. 1955, *ApJ*, 84, 120

Roach, F.E. & Meinel, A. 1961, *ApJ*, 133, 228

Röser, S. & Staude, J. 1978, *AA*, 67, 381

Schubert, G. & Walterscheid, R.L. 1999, in *Allen's Astrophysical Quantities*, Ed. A.N. Cox, (Springer-Verlag: New York), 257

Schiffer, R. 1985, *AA*, 148, 347

Schmidtke, G. 1985, *J. Atmosph. Terrest. Phys.*, 47, 147

Sekera, Z. 1952, *Tables Relating to Rayleigh Scattering of Light in the Atmosphere*, UCLA, Dept. of Meteorology, Sci. Report No. 3.

Sekera, Z. & Ashburn, E.V. 1953, *Tables Relating to Rayleigh Scattering in the Atmosphere*, U.S. Naval Ordnance Test Station, Inyokern, Nav. Ord. Report 2061

Slanger, T.G. & Huestis, D.L. 1981, *J. Geophys. Res.*, 86, 3551

Staude, H.J. 1975, *A&A*, 39, 325

Stone, R.P.S. & Baldwin, J.H. 1983, *MN*, 204, 347

Taylor, B.J. 1984, *ApJS*, 54, 259

van de Hulst, H.C. 1952, in *The Atmospheres of Earth and Planets*, Ed. G.P. Kuiper, (Univ of Chicago Press: Chicago), 52

van Rhijn, P.J. 1924, *Bull Astr. Inst. Netherlands*, 2, 75

van Rhijn, P.J. 1925, *Pub. Gron. Ast. Obs.*, No. 43

Wainscoat, R.J., Cohen, M., Volk, K., Walker, H.J. & Schwartz, D.E. 1992, 83, 111

Weinberg, J.L. 1964, *Ann. Astrophys.*, 27, 718

Weiss-Wrana, K. 1983, *AA*, 126, 240

Wolstencroft, R.D. & van Breda, I.G. 1967, *ApJ*, 147, 255

Zombeck, M.V. 1990, *Handbook of Space Astronomy and Astrophysics*, 2nd ed., (Cambridge: Cambridge Univ. Press), 104